CO line observations of OH/IR stars in the inner Galactic Bulge: Characteristics of stars at the tip of the AGB

(article starts on next page)

Astronomy & Astrophysics

CO line observations of OH/IR stars in the inner Galactic Bulge: Characteristics of stars at the tip of the AGB[⋆]

H. Olofsson[1], T. Khouri[1], B. A. Sargent[2,3], A. Winnberg[1], J. A. D. L. Blommaert[4], M. A. T. Groenewegen[5], S. Muller[1], J. H. Kastner[6], M. Meixner[7], M. Otsuka[8], N. Patel[9], N. Ryde[10], and S. Srinivasan[11]

[1] Department of Space, Earth and Environment, Chalmers University of Technology, Onsala Space Observatory, 43992 Onsala, Sweden
e-mail: hans.olofsson@chalmers.se
[2] Space Telescope Science Institute, 3700 San Martin Drive, Baltimore, MD 21218, USA
[3] Center for Astrophysical Sciences, The William H. Miller III Department of Physics and Astronomy, Johns Hopkins University, Baltimore, MD 21218, USA
[4] Astronomy and Astrophysics Research Group, Department of Physics and Astrophysics, Vrije Universiteit Brussel, Pleinlaan 2, 1050 Brussels, Belgium
[5] Koninklijke Sterrenwacht van België, Ringlaan 3, 1180 Brussels, Belgium
[6] Chester F. Carlson Center for Imaging Science, School of Physics & Astronomy, and Laboratory for Multiwavelength Astrophysics, Rochester Institute of Technology, Rochester, NY 14623, USA
[7] Stratospheric Observatory for Infrared Astronomy/USRA, NASA Ames Research Center, MS 232-11, Moffett Field, 94035 CA, USA
[8] Okayama Observatory, Kyoto University Honjo, Kamogata, Asakuchi, Okayama 719-0232, Japan
[9] Center for Astrophysics – Harvard & Smithsonian, 60 Garden Street, MS 78, Cambridge, MA 02138, USA
[10] Lund Observatory, Department of Astronomy and Theoretical Physics, Lund University, Box 43, 22100 Lund, Sweden
[11] Instituto de Radioastronomía y Astrofísica, Universidad Nacional Autónoma de México, Morelia, Michoacán 58089, Mexico

ABSTRACT

Context. OH/IR stars are examples of late stellar evolution on the asymptotic giant branch (AGB), and they are, as such, important objects to study. They are also excellent probes of stellar populations, in particular in regions of high interstellar extinction such as the central regions of our Galaxy.

Aims. Our goal is to characterise the stellar and circumstellar properties of high-mass-loss-rate OH/IR stars in the inner Galactic Bulge using the Atacama Large Millimeter/submillimeter Interferometer (ALMA).

Methods. Rotational lines of ^{12}CO and ^{13}CO, as well as a millimetre-wave continuum, have been observed for a sample of 22 OH/IR stars in directions within $2°$ of the Galactic Centre. Photometry data ($\approx$1–30 μm) have been gathered from the literature to construct spectral energy distributions (SEDs) and to determine pulsational variability. Radiative transfer models have been used to interpret the line and photometry data.

Results. All stars in the sample were detected in at least one CO line, and eight objects were detected in 324 GHz continuum. Based on luminosity criteria, the sample is divided into 17 objects that most likely lie within the inner Galactic Bulge, and five objects that are most likely foreground objects. The median luminosity of the inner-Galactic-Bulge sub-sample, 5600 $L_\odot$, corresponds to an initial mass in the range 1.2–1.6 $M_\odot$, indicating that these inner-Galactic-Bulge OH/IR stars descend from solar-type stars. The objects in this sub-sample are further divided into two classes based on their SED characteristics: Eleven objects have SEDs that are well matched by models invoking dust envelopes extending from a few stellar radii and outwards, while six objects are better modelled as having detached dust envelopes with inner radii in the range 200–600 au and warmer central stars. The former objects have periodic variability, while the latter objects are predominantly non-periodic. The median gas-mass-loss rate, gas terminal expansion velocity, gas-to-dust mass ratio, and circumstellar ^{12}CO/^{13}CO abundance ratio have been estimated to be 2×10^{-5} $M_\odot$ yr^{-1}, 18 km s^{-1}, 200 (excluding the sources with detached dust envelopes, which show markedly lower gas-to-dust ratios), and 5, respectively, for the inner-Galactic-Bulge sub-sample. All line brightness distributions are resolved at an angular scale of $\approx0''.15$, but only two objects show a structure in their circumstellar envelopes at our resolution and sensitivity. In both cases, this structure takes the form of a cavity and a bipolar morphology.

Conclusions. The inner-Galactic-Bulge sub-sample consists of high mass-loss-rate stars that descend from solar-type progenitors and that lie near the tip of the AGB. Some of the sample stars may have recently ceased mass loss and, hence, have begun to evolve beyond the AGB, as evidenced by a change in circumstellar characteristics and indications of warmer central stars. The inferred very low stellar ^{12}C/^{13}C isotope ratios are indicative of CNO-cycle nuclear processing, and they are most likely established at the surfaces of the stars during the first dredge-up on the red giant branch since these stars are not expected to experience hot-bottom burning. The inner-Galactic-Bulge OH/IR stars studied here constitute an excellent sample of equidistant objects for the purpose of understanding the evolution of the mass-loss-rate characteristics at the tip of the AGB.

Key words. AGB and post-AGB – circumstellar matter – stars: mass-loss – radio lines: stars

---

1. Introduction

In the early 1970s, point-like objects with two main observational characteristics were found: unusually strong 'satellite' 1612 MHz maser line emission from hydroxyl (OH), compared to that of the 'main lines' at 1665 and 1667 MHz, and a double-peaked line profile with sharp outer edges and inner edges decreasing more slowly towards the systemic velocity (e.g. Wilson & Barrett 1972; Winnberg et al. 1973; Caswell & Haynes 1975; Bowers 1978). As data on these objects were gathered, the suspicion that they are highly evolved stars of solar type strengthened (Johansson et al. 1977; Baud et al. 1981). The association with highly reddened sources provided conclusive evidence that these objects are stars that lie at the upper end of the asymptotic giant branch (AGB) (Baud & Habing 1983; Habing 1996). Optically thick circumstellar envelopes (CSEs), produced by intense mass loss, led to high extinction at optical wavelengths. These objects were given the name OH/IR stars. The presence of OH means that they must be of the O-type, that is O is more abundant than C in number (in the CSE, and by inference also in the stellar atmosphere). In fact, mass-losing red supergiants also exhibit these characteristic OH 1612 MHz line profiles (Cohen et al. 1987).

Goldreich & Scoville (1976) presented the first physical-chemical model of an AGB CSE in which the OH molecules are formed through dissociation of circumstellar H_2O by interstellar UV radiation. The OH molecules subsequently become excited by infrared radiation from dust at 35 and 53 μm to produce strong maser emission in the satellite line at 1612 MHz (Elitzur et al. 1976). Additional work on circumstellar OH chemistry and excitation has been done by Huggins & Glassgold (1982), Deguchi (1982), and Netzer & Knapp (1987), for instance.

The fact that the OH maser emission propagation is unaffected by interstellar extinction has made the OH/IR stars important probes of both stellar evolution and galactic structure. Large surveys have been performed over the years (e.g. Eder et al. 1988; te Lintel Hekkert et al. 1991; Lindqvist et al. 1992b; Le Squeren et al. 1992; Engels & Lewis 1996; Sevenster et al. 1997; Sjouwerman et al. 1998; see Chen et al. 2001 for a summary of OH observations of OH/IR stars). Until today, more than a thousand OH/IR stars have been detected in the Milky Way. In addition, about a dozen have been detected in the Large Magellanic Cloud (Goldman et al. 2017).

The penetrating ability of the long-wavelength emission has been particularly important for studies of stars in the Galactic Plane, the Galactic Bulge (GB; defined here as in Barbuy et al. 2018 as the region within $|\ell| \lesssim 10°$ and $|b| \lesssim 10°$ of the Galactic Centre (GC)), and the GC. Sevenster et al. (1997) detected more than 250 objects with OH/IR star characteristics in the GB, with ≈80 of them lying within the inner GB (within ≲2° of the GC; sometimes called the nuclear bulge (Mezger et al. 1996) or a disky pseudobulge (Kormendy & Bender 2019)), and at higher sensitivity Lindqvist et al. (1992b) and Sjouwerman et al. (1998) detected ≈190 OH/IR objects within 0.3° of the GC. van der Veen & Habing (1990) concluded that the OH/IR stars in the GB are dominated by ≈1.0–1.4 $M_\odot$ progenitor stars with an age >7 Gyr. Wood et al. (1998) used photometry for a sample of OH/IR stars within 0.7° of the GC to conclude that closer to the GC there are also younger AGB stars belonging to an intermediate-age population. This is a conclusion supported by the study of Mira variables in the inner Galaxy by Groenewegen & Blommaert (2005). They found an inner-GB population of age 1–3 Gyr, and an even younger population

closer to the GC, ≈1 Gyr (see also van Loon et al. 2003). In general, it appears that the OH/IR stars cover the full mass range of AGB stars, from ≈1 to ≈8 $M_\odot$ (Habing 1996). Apart from this, these OH/IR stars are not particularly well characterised, although near-IR spectroscopic work is now making good progress (Schultheis et al. 2020).

The OH maser emission provides interesting insights for studying OH/IR stars, but only brings (at best) order-of-magnitude estimates of the mass-loss rate, and no information on elemental isotopic ratios, such as $^{12}C/^{13}C$, which are key signposts of stellar evolution. Observations of rotational lines from carbon monoxide (CO) have proven to be essential in this context (e.g. Schöier & Olofsson 2001; De Beck et al. 2010; Ramstedt & Olofsson 2014). The first major CO-based study of OH/IR stars were done by Heske et al. (1990) on 13 objects. The major conclusions were that the estimated mass-loss rates from the CO lines (using a semi-empirical formula) were much lower than those estimated from dust continuum, dust features, and OH maser emission, and that the $J = 2–1/J = 1–0$ line intensity ratios were unexpectedly high. A possible explanation for both results would be a recent increase in mass-loss rate, the start of a superwind. Such a conclusion was further strengthened by the work of Justtanont & Tielens (1992) and Justtanont et al. (1994, 1996). However, the mass-loss-rate-estimate methods used in these papers had substantial uncertainties. In a recent paper based on ALMA CO observations of two OH/IR stars, Decin et al. (2019) concluded that a fair fraction of the dust is assembled into an equatorial density enhancement due to the binary nature of the objects, and that this would explain the discrepant mass-loss rates found in previous papers. This explanation was extrapolated to all OH/IR stars, concluding that they reach maximum mass-loss rates of the order a few times 10^{-5} $M_\odot$ yr^{-1}. In a study of a sample of five OH/IR stars, Delfosse et al. (1997) found that the circumstellar $^{12}CO/^{13}CO$ abundance ratios were very low, about 3.5 (compared to 89 in the solar photosphere (Clayton & Nittler 2004) and 68 in the ISM (Milam et al. 2005)). Arguments were given that these reflect the stellar $^{12}C/^{13}C$ ratios and that the low values, close to the equilibrium value of the CNO cycle, were due to the hot-bottom-burning process at the end of the AGB (Karakas & Lugaro 2016). The consequence being that the stars in their sample are more massive than about 4 $M_\odot$.

A detailed study of the mass-loss characteristics of OH/IR stars based on observations of CO rotational lines is therefore warranted. In particular, a sample of equidistant objects can be formed by selecting OH/IR stars in the inner Galaxy. However, the presence of ubiquitous interstellar CO along the lines-of-sight complicates such observations. The first OH/IR stars detected in CO line emission towards the GB and GC were therefore restricted to high-velocity objects with emission well outside the velocity range of interstellar CO line emission (2 objects; Winnberg et al. 1991), or objects well outside the regions of highest extinction (7 objects; Blommaert et al. 2018). The ability of interferometers to filter out extended emission was used to increase the number of objects detected in CO line emission in higher-extinction regions (Winnberg et al. 2009; Sargent et al. 2013), bet led to only four new detections. In this paper, we present observations of both ^{12}CO and ^{13}CO lines performed with the Atacama Large Millimeter/submillimeter Array (ALMA) that substantially increase the number of OH/IR stars detected in circumstellar CO line emission in the inner GB. In total, 22 stars were observed, all of them were detected in at least one CO line.

2. The sample

The objects were selected among the OH/IR stars detected in OH 1612 MHz emission by Lindqvist et al. (1992b), Sevenster et al. (1997), and Sjouwerman et al. (1998) within about 2° of the GC (corresponding to ≲300 pc), that is the inner GB. Stars in directions where the CO($J = 2–1$) line emission obtained by Sawada et al. (2001) exceeds 2.2 K in intensity were omitted in order to minimise the effect of interstellar CO line emission along the line of sight. For the rest, GRAMS models of M-type AGB stars (Sargent et al. 2011) were fitted to extinction-corrected spectral energy distributions (SEDs; the SEDs and the method of extinction correction were different than the ones eventually adopted in this paper)[1]. The 22 objects with the largest dust production rates were eventually selected to form the sample. The objects are listed with their OH/IR identifications in Table 1, and they are shown overlaid on a 70 μm image in Fig. 1 (the numbering of the sources introduced here is used in the tables throughout this paper). In this way, the sample is biased towards the highest-mass-loss-rate OH/IR objects in the inner GB that are not severely affected by interstellar extinction (as a consequence only five of our objects lie within 0.3° of the GC, corresponding to ≲40 pc). Our sources must be regarded as the 'tip of the iceberg' since Sevenster et al. (1997) found about 80 OH/IR objects within 2° of the GC, and Lindqvist et al. (1992b) and Sjouwerman et al. (1998) in much deeper surveys found about 190 such objects within 0.3° of the GC.

We have adopted a distance to the GC of 8.2 kpc, based on the recent estimate of the distance to the black hole in the GC by the GRAVITY Collaboration (GRAVITY Collaboration 2019). This measurement has a very small formal error ($8178 \pm 13_{\text{stat}} \pm 22_{\text{sys}}$ pc), but we note that our sources will be spread out along the line of sight even if they are located in the inner GB. None of our sources have a measured reliable parallax in *Gaia* EDR3 (Gaia Collaboration 2021).

3. Observational data

3.1. ALMA data

The ALMA dataset consists of three different tunings to cover the ^{12}CO $J = 2–1$ line in Band 6 (≈230 GHz) and the ^{12}CO and ^{13}CO $J = 3–2$ lines in Band 7 (≈345 and 330 GHz, respectively). The ^{12}CO tunings were observed in one execution each in October 2016, with a fast snapshot observation of about 12 s on each of the 22 targets. The ^{13}CO tuning was observed three times, twice in October 2016 and once in July 2017, with a longer integration time of about 50 s per target for each execution. The total amount of on-source observing time was only about an hour

---

[1] Photometric data for the SEDs were taken from 2MASS (J, H, and K_{s}), *Spitzer*-IRAC (3.6, 4.5, 5.8, and 8.0 μm), *Spitzer*-MIPS (24 μm), WISE bands W1 (3.4 μm), W2 (4.6 μm), W3 (12 μm), and W4 (22 μm), and Akari (9 and 18 μm). Extinction-correction was performed in the following way: all targets were assumed to have an intrinsic H–K colour of 0.25, as assumed for red giants in the fields observed by Wood et al. (1998). If a given target had H and K photometry (from 2MASS; in a few cases DENIS K_{s} data were used), E(H–K) could be computed directly; if not, the average of the values where E(H–K) could be computed directly was adopted. The extinction in K was estimated from $A_{\text{K}} = 1.5E$(H–K) (Wood et al. 1998). Finally, the extinction law of McClure (2009) was used to determine the extinction at all the other photometric bands for objects where $A_{\text{K}} > 1$.

Table 1. Sample sources.

Source [a]	α(J2000) [b] (h:m:s)	δ(J2000) [b] (°:′:″)
1 - OH358.083+0.137	17:40:26.49	–30:29:38.9
2 - OH358.162+0.490	17:39:14.93	–30:14:24.3
3 - OH358.235+0.115	17:40:54.14	–30:22:38.1
4 - OH358.505+0.330	17:40:43.37	–30:02:04.7
5 - OH359.140+1.137	17:39:07.70	–29:04:03.0
6 - OH359.149−0.043	17:43:44.96	–29:41:00.9
7 - OH359.220+0.163	17:43:06.74	–29:30:56.9
8 - OH359.233−1.876	17:51:12.13	–30:33:40.5
9 - OH359.467+1.029	17:40:20.32	–28:50:55.3
10 - OH359.543−1.775	17:51:32.08	–30:14:36.3
11 - OH359.664+0.636	17:42:20.47	–28:53:21.4
12 - OH359.745−0.404	17:46:35.66	–29:21:51.5
13 - OH359.805+0.200	17:44:22.27	–28:59:54.5
14 - OH359.826+0.153	17:44:36.46	–29:00:19.8
15 - OH359.902+0.061	17:45:08.81	–28:59:16.7
16 - OH0.173+0.211	17:45:12.43	–28:40:44.4
17 - OH0.221+0.168	17:45:29.41	–28:39:35.6
18 - OH0.548−0.059	17:47:08.98	–28:29:56.3
19 - OH0.739+0.411	17:45:46.66	–28:05:29.3
20 - OH1.095−0.832	17:51:26.77	–28:25:37.1
21 - OH1.221+0.294	17:47:21.74	–27:44:23.9
22 - OH1.628+0.617	17:47:03.91	–27:13:30.9

Notes. [a] Source names are taken from Lindqvist et al. (1992b), Sevenster et al. (1997), or Sjouwerman et al. (1998). The SIMBAD identifiers for OH359.805+0.200 and OH359.826+0.153 are OH359.80+0.20 and OH359.800+0.165, respectively. [b] Coordinates determined from the ^{13}CO($J = 3–2$) data presented in this paper, except for OH359.149−0.043 and OH0.173+0.211 where the near-IR and ^{12}CO($J = 2–1$) positions are given, respectively.
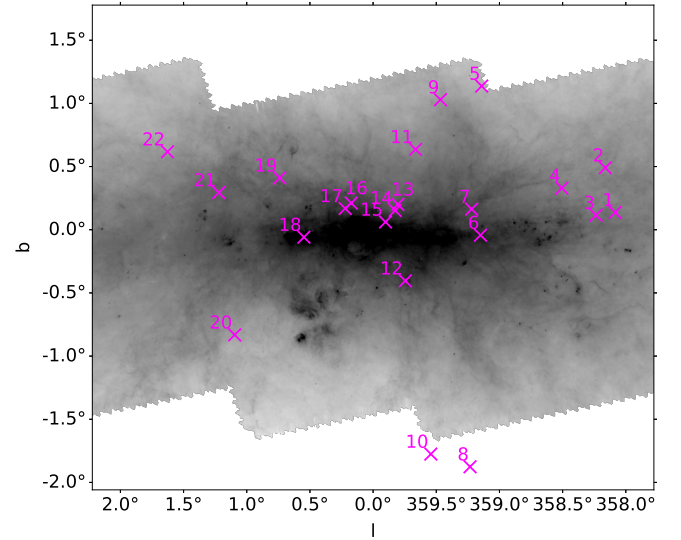
Fig. 1. Positions of the sources marked as crosses on a 70 μm image obtained with the PACS instrument on the *Herschel* Space Observatory. The numbers refer to the source identifications in Table 1.

for the whole project. A journal of the observations is given in Table 2.

The observations were performed in array configurations with baselines ranging between ≈20 m to 2–3 km. The achieved

Table 2. Journal of the observations.

Band	Line	Date of observation	N_{ant} [a]	B_{min} / B_{max} [b] (m km^{-1})	PWV [c] (mm)	Flux calibrator [d] (Jy)
B6	^{12}CO($J=2$–1)	04 Oct 2016	41	18/3.1	0.8–1.3	J1924−2914 (3.45 ± 0.06)
B7(a)	^{12}CO($J=3$–2)	11 Oct 2016	41	18/3.1	1.2–1.3	J1733−1304 (1.0 ± 0.2)
B7(b)	^{13}CO($J=3$–2)	13 Oct 2016	41	18/3.1	0.6–0.8	J1924−2914 (2.68 ± 0.07)
		15 Oct 2016	42	18/1.8	0.7–0.9	J1924−2914 (2.99 ± 0.58)
		04 Jul 2017	45	21/2.6	0.5–0.6	J1733−1304 (1.24 ± 0.05)

Notes. [a] Number of 12 m antennas in the array. [b] Minimum and maximum projected baselines. [c] Amount of precipitable water vapour in the atmosphere. [d] Flux density at the corresponding CO line frequency as retrieved from the ALMA flux monitoring database.

synthesised beams (θ_{b}, the full width at half maximum, FWHM) vary, but are typically about 0''16–0''18 in Band 6 and 0''11–0''17 in Band 7. The maximum recoverable angular scales (MRSs) are ≈2''5 (the 230 GHz data), ≈1''5 (the 330 GHz data), and ≈1'' (the 345 GHz data).

For all tunings, the correlator was set up with one 1.875 GHz spectral window centred on the relevant CO line, with 1920 channels separated by 0.977 MHz, and three additional 2 GHz spectral windows with 128 channels and a coarser spacing of 15.625 MHz for continuum measurements (these spectral windows have no strong spectral lines that will affect the flux density estimates). For the continuum this means three measurements with 6 GHz bandwidth centred at the effective frequencies of 222, 324, and 339 GHz for each source. After Hann smoothing[2], the native velocity resolution for the CO spectral windows is between 0.8 and 1.3 km s^{-1}. For the continuum windows, the velocity resolution is between 27 and 40 km s^{-1}. For analysis, the final CO line velocity resolution was set to 5 km s^{-1}.

The calibration was done following the ALMA standard procedures. The bandpass response of the antennas was calibrated on the quasar J1924−2914. The flux calibration was done using the quasars J1924−2914 or J1733−1304, which are regularly monitored by ALMA. The flux accuracy is expected to be within the 5–20% range (see Table 2). The gain (phase and amplitude) calibration was always performed on the quasar J1744−3116.

The data were reduced using different versions of the Common Astronomy Software Applications package (CASA; McMullin et al. 2007). After corrections for the time and frequency dependence of the system temperatures, and rapid atmospheric variations at each antenna using water vapour radiometer data, bandpass and gain calibration were done. Imaging was done using the CASA `tclean` algorithm. The final line images were created using Briggs weighting with a robust parameter of 0.5. This resulted in beam sizes of 0''19 and 0''14 for the Bands 6 and 7 data, respectively. The ^{13}CO $J=3$–2 data have the highest sensitivity, the rms noise per channel in the images is ≈4 mJy beam^{-1} at 5 km s^{-1} resolution. The corresponding values for the ^{12}CO $J=2$–1 and 3–2 data are ≈9 and 24 mJy beam^{-1}, respectively. The continuum rms values are ≈0.23 mJy beam^{-1}, 0.13 mJy beam^{-1}, and 0.65 mJy beam^{-1} at 222, 324, and 339 GHz, respectively.

The presence of interstellar CO line emission along the line of sight occasionally makes it difficult to isolate the circumstellar emission. In such cases, we rejected visibility data

from the shortest baselines, up to 50 m. Eliminating the shortest baselines, ≤50 m (and those are in the far minority of all the baselines) will effectively suppress any extended emission on scales larger than 5–10''. Excluding data from baselines longer than this leads to a loss of flux density and poorer S/N. The effect of interstellar emission contamination is less for the ^{13}CO($J=3$–2) line due to the fact that the circumstellar ^{13}CO/^{12}CO abundance ratios of O-type AGB stars are in general (much) higher than the interstellar values (Milam et al. 2005; Ramstedt & Olofsson 2014). In the end, omission of short-baseline data were used for four objects in this line. In the case of the ^{12}CO lines this method was used for nine sources, but here the isolation of the circumstellar emission was guided by the ^{13}CO results.

The determinations of source positions and sizes of the line brightness distributions are done based on images integrated over the velocity range of the circumstellar line. For the majority of the sources, the line brightness distribution is centrally peaked and eventually fades out into the noise. Hence, the sizes of the molecular envelopes cannot be determined from our data, and we report the FWHM (deconvolved with the synthesised beam) of a two-dimensional Gaussian fitted to the velocity-integrated brightness distribution. The location of the peak of the Gaussian fit gives the source position. We estimate the astrometric accuracy to be better than 0''1.

The line profiles were extracted over an aperture, centred on the peak of the brightness distribution, larger than the estimated FWHM of the brightness distribution, normally 2–3 times larger. The size is set to recover as much as possible of the line flux density, while maintaining an as high as possible S/N and suppressing the influence from the interstellar CO line emission. The uncertainties in the flux densities are affected by a combination of the S/N, the presence of interstellar CO line emission, and the size of the aperture used, and thus difficult to determine in detail. We estimate for the ^{13}CO($J=3$–2) emission that for lines stronger than 0.2 Jy the uncertainty is about 10%, while for lines weaker than 0.1 Jy the uncertainty increases to about 50% for the weakest lines. To this should be added the possible amount of resolved-out flux as discussed in Sect. 6.4. For the ^{12}CO lines the uncertainty in the flux density estimate is about 10% for lines stronger than 1.0 and 2.0 Jy for the $J=2$–1 and 3–2 lines, respectively, and below 0.4 and 1.0 Jy the uncertainties increase to about 50% for the weakest $J=2$–1 and 3–2 lines, respectively. Flux densities, centre velocities (in the local standard of rest frame), and expansion velocities were determined through fitting the line shape function

---

[2] A smoothing procedure introduced by the Austrian meteorologist Julius von Hann; often referred to as hanning smoothing in astronomical literature.

$$S(v) = S(v_{\mathrm{c}}) \left[1 - \left(\frac{v - v_{\mathrm{c}}}{v_{\infty}} \right)^2 \right]^{\beta} \tag{1}$$

to the data, so that $\beta = 1$ means a parabolic, $\beta = 0$ a flat-topped, and $\beta < 0$ a double-peaked line shape. The uncertainties in the expansion and centre velocities depend on the S/N and the presence of interstellar CO line contamination, and are estimated to be about ± 1.5 and $\pm 1 \, \text{km s}^{-1}$, respectively for the $^{13}\text{CO}(J = 3-2)$ data. The corresponding values for the $^{12}\text{CO}(J = 2-1)$ and $^{12}\text{CO}(J = 3-2)$ data are about ± 2 and $\pm 1.5 \, \text{km s}^{-1}$ and about ± 3 and $\pm 2 \, \text{km s}^{-1}$, respectively.

The $^{12}\text{CO}(J = 3-2)$ setting also allowed detection of the $\text{H}^{13}\text{CN}(J = 4-3)$ line at 345.3398 GHz. Three sources were detected, and the line profile results were extracted in the same way as for the CO lines. The uncertainties in the line characteristics are the same as those of the $^{12}\text{CO}(J = 3-2)$ line.

The continuum brightness distributions are sharply peaked and we determine their sizes, positions, and flux densities (and their associated uncertainties) by fitting two-dimensional Gaussians to the data in the image plane. The results are summarised in Table A.5. There is likely to exist also low-surface-brightness, extended dust emission, but it is effectively resolved out by the interferometer due to the small MRSs of our data, about 1–2.5″. Since the brightness distributions for the detected sources are comparable to the size of the synthesised beam, we use the rms flux density per beam in the image to estimate the upper limit for a non-detection.

3.2. Photometry and variability

We gathered photometric data from archives through the VizieR Photometry viewer and the NASA/IPAC infrared science archive. The specific catalogues used were the ISOGAL Point Source Catalogue (Omont et al. 2003), the Midcourse Space Experiment Point Source Catalog Version 2.3 (Egan et al. 2003), OH-selected AGB and post-AGB objects (Sevenster 2002), the UKIDSS-DR6 Galactic Plane Survey (Lucas et al. 2008), the MIPSGAL 24 μm point source catalogue (Gutermuth & Heyer 2015), AllWISE (Cutri et al. 2013), the Pan-STARRS release 1 (PS1) Survey – DR1 (Chambers & Pan-STARRS Team 2016), the Hi-GAL inner Milky Way: $+68 \geq \ell \leq +70$ (Molinari et al. 2016), the Hi-GAL compact source catalogue (Elia et al. 2017), the IRAS PSC/FSC Combined Catalogue (Abrahamyan et al. 2015), Catalog of 24 μm sources toward Galactic Center (Hinz et al. 2009), NOMAD Catalog (Zacharias et al. 2005), the Galactic Legacy Infrared Midplane Survey Extraordinaire (Spitzer Science 2009), AKARI/IRC mid-IR all-sky Survey (Ishihara et al. 2010), and the *Herschel*/PACS Point Source Catalogs (Herschel Point Source Catalogue Working Group et al. 2020). The photometry data used are available at the CDS as tables for each source containing the wavelength, the flux density, its uncertainty, and the reference.

Since the stars in our sample are in the inner GB, interstellar extinction can be very high. We have retrieved the reddening $E(J - K_\text{s})$ towards each source using the results of Gonzalez et al. (2018). The reddening is converted into extinction in the K_s band, A_{K_s} given in Table 4, and extrapolated up to 8 μm using the relationships provided by Nishiyama et al. (2009). In the range 8–30 μm we use the results of Wang et al. (2015) and Xue et al. (2016). No corrections were applied for data at wavelengths longer than 30 μm because $A_\lambda / A_{K_\text{s}}$ is expected to be lower than 0.2, which would imply relatively small corrections even for the higher-extinction sources.

Pulsation periods have been estimated using data from the VISTA Variables in the Vía Láctea (VVV) ESO Public Survey (Minniti et al. 2010), and data from the combined Wide-field Infrared Survey Explorer (WISE) (Wright et al. 2010) and the

Near-Earth Object WISE (NEOWISE; Mainzer et al. 2011, 2014). Using preliminary coordinates for the sources the NIR counterpart was identified in the VVV images. In all cases the coordinates of the NIR counterpart coincided with the ALMA counterpart at the level of 0″1. For the counterpart, the available data in the Z (0.88 μm), Y (1.02 μm), J (1.25 μm), H (1.64 μm), and K_s (2.15 μm) filters were retrieved. In $ZYJH$ these are typically four or less observations, while dozens of data points are available in K_s. The K_s-band light curves have been analysed using the codes and methodology outlined in Groenewegen et al. (2020) assuming a single period. For the WISE data a very similar approach was adopted to analyse the light curves in the W1 (3.4 μm) and W2 (4.6 μm) bands, as outlined in Groenewegen (2022). The results, including the adopted period are collected in Table 3 that also cites periods found in the literature.

Pulsation periods could be determined for 13 objects. In one case, the period was taken from the literature. One object shows non-Mira multi-periodic variability. In a few stars saturation in the K or WISE bands are an issue, but only in one case did this mean that a period could not be determined. The remaining six stars show scatter beyond what is expected based on the error in the individual measurements, but none of them show a periodic behaviour, that is they are classified as non-periodic.

4. Observational results

4.1. The ^{12}CO and ^{13}CO lines

The $^{13}\text{CO}(J = 3-2)$ data have the highest S/N and are less affected by contamination from interstellar CO line radiation (as explained above). Consequently, we start the discussion with this line in which we detect 21 (out of 22) sources. Figure 2 shows the $^{13}\text{CO}(J = 3-2)$ images (obtained by integrating the brightness distribution over the velocity range of the line) and Fig. 3 shows the spectra. For the majority of the sources (19), the brightness distributions are centrally peaked and no source structure is discernible. One source, OH359.149−0.043, shows a very strange brightness distribution (which is repeated also in the two ^{12}CO lines). Two sources with resolved structure are discussed below. The observational results are summarised in Appendix A.1.

The ^{12}CO $J = 2-1$ and 3–2 lines are detected towards 22 and 20 sources, respectively. In quite a number of these cases, the detections would have been characterised as tentative if it were not for the detection of the $^{13}\text{CO}(J = 3-2)$ line. OH0.173+0.211 was detected in only the $^{12}\text{CO}(J = 2-1)$ line[3]. Its brightness distribution is centrally peaked and no source structure is discernible. Tables with the observational results are presented in Appendix A.1. The images and spectra for these lines are shown in Appendices A.2 and A.3, respectively.

The ^{13}CO positions are given in Table 1, and their uncertainties (including the astrometric uncertainty, Sect. 3.1) are estimated to be 0″1 (3σ) for the highest S/N data, increasing to 0″2 (3σ) for the poorest S/N data. All brightness distributions peak in the vicinity of a near-IR source in the VVV data. The median and maximum offsets between the $^{13}\text{CO}(J = 3-2)$ and near-IR positions are 0″11 and 0″23, respectively. The only offset larger than the combined uncertainties is obtained for OH358.505+0.330, the source with the largest resolved structure in the CO lines. The median and maximum offsets between

---

[3] The position used for the ALMA observations, the one given by Sjouwerman et al. (1998), is about 6″ north of the position of the OH source (Lindqvist et al. 1992b), but still within the half power width of the primary beam.

Table 3. Pulsation periods of the sources.

Source	P_{K_s} (days)	σ_{K_s} (days)	P_{W1} (days)	σ_{W1} (days)	P_{W2} (days)	σ_{W2} (days)	$P_{literature}$ (days)	Ref.	$P_{adopted}$ (days)	Comment
1 - OH358.083+0.137	...	...	...	...	...	...	...		...	Scatter, not periodic
2 - OH358.162+0.490	...	...	1228	29	1272	60	1150, 1120	2, 3	1230	Scatter in K
3 - OH358.235+0.115	...	...	...	...	...	...	874	4	874	Saturation in K and WISE
4 - OH358.505+0.330	...	...	...	...	...	...	...		...	Scatter, not periodic
5 - OH359.140+1.137	...	...	1219	104	989	19	...		1000	Very low-amplitude variability
6 - OH359.149−0.043	...	...	...	...	...	...	...		...	Scatter. not periodic
7 - OH359.220+0.163	...	...	...	...	...	...	...		...	Scatter in K. too few datapoints in WISE
8 - OH359.233−1.876	...	...	...	...	...	...	...		...	Scatter in K. too few datapoints in WISE
9 - OH359.467+1.029	604	3	604	1.3	605	2.4	...		605	
10 - OH359.543−1.775	...	...	...	...	...	...	790	5	...	Multi-periodic, non-Mira
11 - OH359.664+0.636	...	...	538	3.3	581	4.3	...		550	Scatter in K
12 - OH359.745−0.404	733	4	714	4.4	732	5.0	806, 766	1, 6	730	
13 - OH359.805+0.200	533	10	488	3.8	501	6.5	...		500	
14 - OH359.826+0.153	501	3	483	2.1	489	4.3	493, 510	1, 6	500	
15 - OH359.902+0.061	586	13	611	3.4	588	5.1	558, 572, 550, 580	1, 7, 7, 8	590	
16 - OH0.173+0.211	512	4	510	5.5	516	6.8	...		512	
17 - OH0.221+0.168	664	4	663	4.7	662	3.6	697	1	663	
18 - OH0.548−0.059	...	...	...	...	...	...	...		...	Scatter, not periodic
19 - OH0.739+0.411	577	10	557	2.8	602	2.8	...		570	
20 - OH1.095−0.832	...	...	...	...	...	...	...		...	Saturated
21 - OH1.221+0.294	699	3	715	2.0	715	6.8	...		715	
22 - OH1.628+0.617	921	43	827	6.5	839	8.0	...		830	

Notes. Period with error in the K_s (2.15 μm) (Cols. 2, 3), $W1$ (3.4 μm) (Cols. 4, 5), and $W2$ (4.6 μm) (Cols. 6, 7) bands. Column (9): references for periods in the literature quoted in Col. (8): (1) Wood et al. (1998), (2) Le Bertre (1993), (3) Olivier et al. (2001), (4) present work, data from the Bochum Galactic Disk Survey (Hackstein et al. 2015) for source GDS_J1740541-302238, (5) present work, data from OGLE (Soszyński et al. 2013) for source OGLE-BLG-LPV-074942 classified as a semi-regular variable with principal period of 78.2 days, (6) Braga et al. (2019; also based on VVV data, but fewer data points than in the present study), (7) Glass et al. (2001; two periods from data in overlapping fields), (8) Matsunaga et al. (2009).

the ^{13}CO($J = 3$–2) and the ^{12}CO($J = 2$–1 and 3–2) positions are 0″09 and 0″26 and 0″07 and 0″20, respectively. Half of the ^{13}CO($J = 3$–2) positions are within 0″5 of the OH position, all but two are within 1″0 of the OH position, and the largest offset between the two is 2″2. The uncertainties in the OH positions are significantly larger than those of our CO line data.

The estimated sizes of the ^{13}CO($J = 3$–2) brightness distributions (θ_s) lie in the range 0.2–1″, that is they are all resolved. The ^{12}CO $J = 2$–1 and 3–2 brightness distributions are only marginally larger. For the sources located at the distance of the GC, 1″ corresponds to $\approx 1.2 \times 10^{17}$ cm, or ≈ 8200 au. The implications of these sizes are further discussed in Sect. 6.5.

Two sources, OH358.505+0.330 and OH359.220+0.163, show evidence of resolved structure in the ^{13}CO($J = 3$–2) brightness distribution. In both cases there appears to be a cavity and a bipolar structure surrounding the star, see Fig. 2. For both sources the line with the, by far, highest S/N, the ^{13}CO($J = 3$–2) line, shows a line profile expected from circumstellar thermal line emission, see Fig. 3. Zijlstra et al. (1989) classified OH358.505+0.330 as a planetary nebula (PN) based on a radio continuum detection at 6 cm using the Very Large Array (VLA), although they stated that the detection should be repeated due to a low S/N. More recently, Uscanga et al. (2012) argued that the claimed radio continuum detection is wrong (by looking at VLA archival data), and hence there is presently no evidence that this object is a PN. For OH359.220+0.163 there exists only OH maser observations in the literature. We note here, that for neither of these two objects do we detect 324 GHz continuum emission.

4.2. The H^{13}CN($J = 4$–3) line

The H^{13}CN($J = 4$–3) line was detected in three of our sample objects. The results and spectra are presented in Appendices A.1 and A.3, respectively.

4.3. ALMA continuum measurements

In total eight sources were detected in 324 GHz continuum, five were detected at 222 GHz, and four detected at 339 GHz, see Table A.5. This is fully explained by the lower S/N in the 222 and 339 GHz data. When detections are made in all three bands, the flux densities are consistent with a spectral index α of about 1.5–3 ($S_\nu \propto \nu^\alpha$). Only the upper limits to the 339 GHz flux densities of OH359.233−1.876 and OH0.739+0.411 are surprising, since they are about two times below the flux densities at 324 GHz. We have no explanation for this. There is nothing obviously wrong with the observations of these particular sources. All objects were observed consecutively at 339 GHz, in snap-shot mode, using the same source as phase reference. The images for all sources and frequencies are presented in Appendix A.2. The continuum brightness distributions are significantly smaller than those of the CO lines. Deconvolved FWHMs are comparable to, or smaller than, the beams, $\lesssim 0″15$. The median and maximum offsets between the ^{13}CO($J = 3$–2) and 324 GHz continuum positions are 0″02 and 0″12, respectively (OH359.149−0.043 is excluded in the comparison because of its strange line brightness distribution). The largest offset is found for OH358.162+0.490, a result due to the fact that this source has the apparently
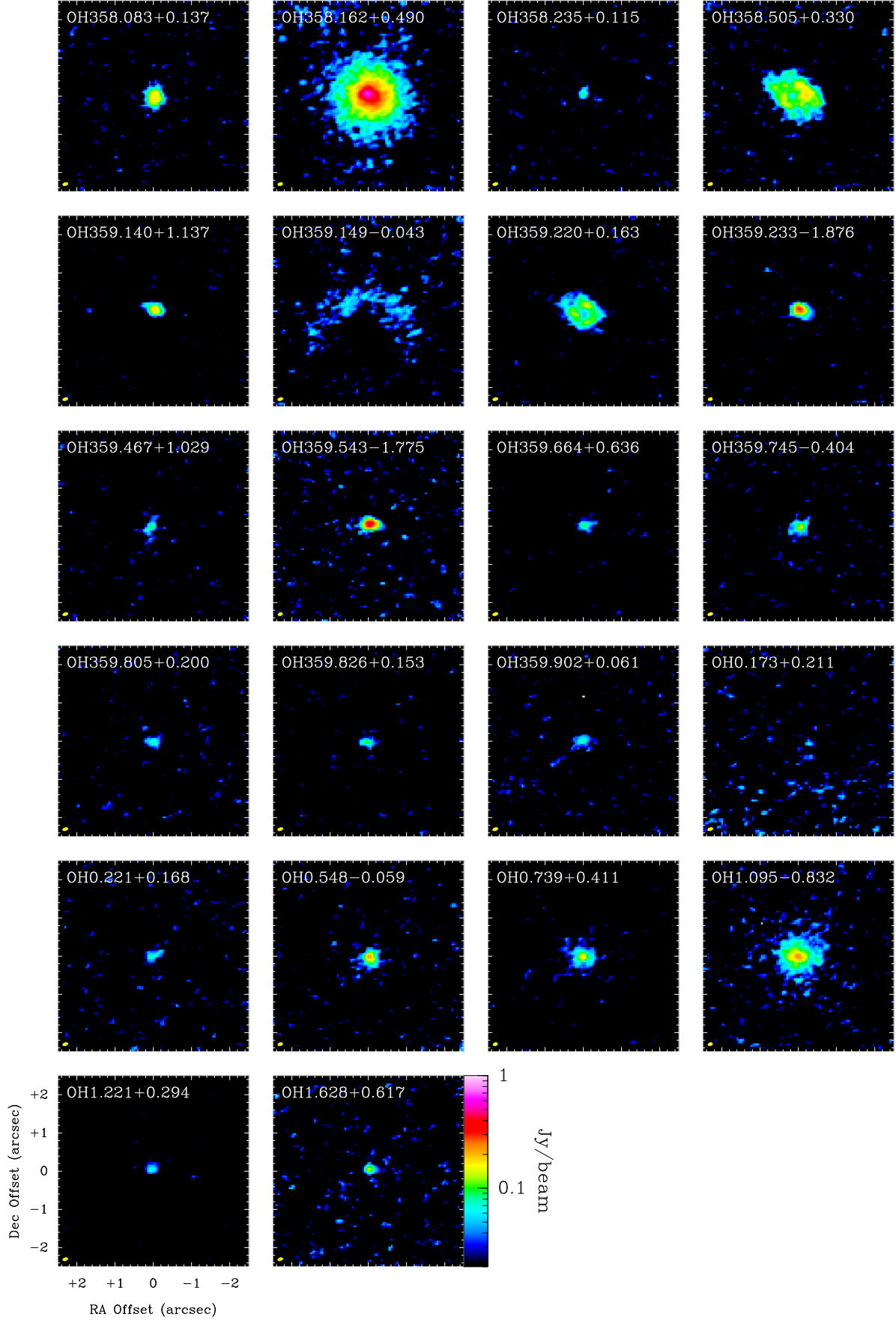
Fig. 2. ^{13}CO($J = 3$–2) brightness distribution integrated over the line for all sources in the sample. A logarithmic scale is used in order to have the same scale for all objects. The synthesised beams are shown in the lower left corner of each panel.
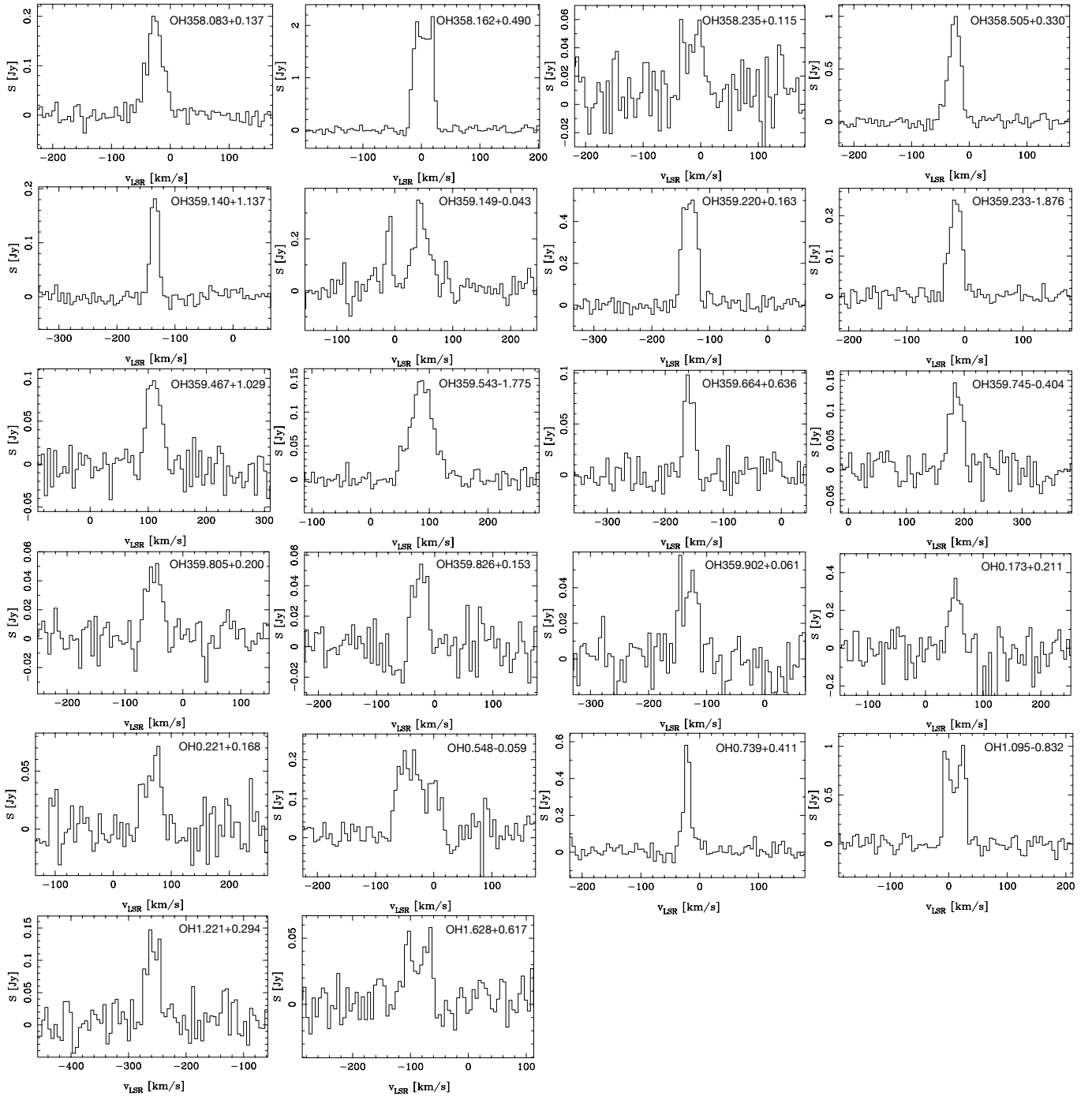
Fig. 3. ^{13}CO($J = 3$–2) spectra at a velocity resolution of 5 km s^{-1}, except for OH0.173+0.211 where the ^{12}CO($J = 2$–1) spectrum is shown.

largest ^{13}CO($J = 3$–2) brightness distribution among the sources detected in 324 GHz continuum. The other offsets are within the combined uncertainties.

A simple calculation shows that the expected continuum flux at 324 GHz from a 2500 K blackbody of luminosity 5000 $L_\odot$ (typical for our sources as shown below) at the distance of the GC would be about 0.04 mJy. This is well below our detection limit, and it means that any detected continuum emission from sources at that distance must be due to circumstellar dust emission. However, this means that there is an issue with resolved-out continuum flux. The reason is that the larger fraction of the total millimetre/submillimetre flux density comes from extended

emission from cold dust, that is from extended low-surface brightness emission which is not seen by the interferometer. The size of the emitting region is likely much larger than the radius of the MRS, $\approx 1''$ at 324 GHz, corresponding to about 8200 au if placed at the GC (a distance covered by an 18 km s^{-1} outflow in about 2200 yr). The high-mass-loss-rate phase may have lasted longer than this, and consequently the dust-CSE may be larger than this. Using the dust radiative transfer modelling (described in Sect. 5.1) we estimate that the measured ALMA flux densities are in general, at least, a factor of two below the true flux densities, that is the reported ALMA flux density is a conservative lower limit to the total flux density for the detected sources.

5. Radiative transfer

5.1. Dust continuum radiation

To reproduce the SED of each source, we calculated radiative transfer models using the code MCMax (Min et al. 2009) assuming spherical symmetry of the dust CSEs. We consider astronomical silicate grains (Ossenkopf et al. 1992) with a number size distribution given by a power law with index −3.5 and minimum and maximum grains sizes equal to 0.001 μm and 1.0 μm, respectively. The spherical dust CSEs were assumed to extend from an inner radius R_{in} to 10 000 au. The former is either determined by the radius at which the dust temperature is 1000 K (as calculated by the code), or as the required inner radius to give a good fit to the data. The latter corresponds to roughly half the ALMA MRS for our observations at the distance of the GC. In this way the SED models should, in principle, be able to reproduce the observed ALMA fluxes. The particular choice of the outer radius does not affect the estimated emission at wavelengths shorter than ≈70 μm, only that at longer wavelengths. The density distribution is proportional to r^{-2}, where r is the radial distance from the central star (corresponding to constant mass-loss rate and expansion velocity). The stellar temperature, $T_\star$, was set to 2500 K initially. The free parameters in the fit are R_{in} (where required), $T_\star$ (where required), and the dust optical depth at 9.7 μm ($\tau_{9.7}$).

In the fitting procedure, we only include photometric points for wavelengths larger than 1 μm because of the large extinction towards some of the sources and the relatively small contribution to the total luminosity of the emission at optical wavelengths. The SED was fitted by eye by varying mainly $\tau_{9.7}$. When an acceptable fit could not be obtained, we varied R_{in}. If necessary, we also increased the stellar temperature to decrease the stellar emission in the near-infrared.

The dust-mass-loss rate is obtained assuming that the expansion velocity of the dust equals that estimated from the observed CO lines. This is a reasonable assumption, since the drift between the dust and the gas is believed to be limited to at most a few km s^{-1} for high-mass-loss-rate objects (Kwok 1975). The stellar luminosity is obtained by integrating the fit to the SED over wavelength and using the distance to the given source.

5.2. CO line radiation

For the line emission analysis, we used a well-tested, non-local-thermodynamic-equilibrium radiative transfer code based on the Monte Carlo method (Bernes 1979; Schöier & Olofsson 2001). We assume a CSE expanding with constant velocity (the terminal gas expansion velocity v_∞), which is formed by a constant and isotropic gas-mass-loss rate ($\dot{M}_g$).

We have observational data for only two rotational lines of ^{12}CO, and this is not enough to put constraints on the radial distribution of the kinetic temperature for each individual source. We have therefore opted for using the same circumstellar model for all sources, the one obtained for the high-mass-loss-rate (10^{-5} $M_\odot$ yr^{-1}) M-type AGB star IK Tau by Ramstedt & Olofsson (2014). In this model, the kinetic temperature law is given by

$$T_k = 940 \left[\frac{4 \times 10^{14}}{r} \right]^{0.9} \text{[K]}, \tag{2}$$

where r is given in cm, and with a lower limit of $T_{min} = 7.5$ K at large radii. In addition to thermal motion of the molecules,

we assume a micro-turbulent velocity field of 1 km s^{-1}. Likewise, Ramstedt & Olofsson (2014) derived the following dust temperature law for IK Tau,

$$T_d = 580 \left[\frac{4 \times 10^{14}}{r} \right]^{0.4} \text{[K]}, \tag{3}$$

where r is given in cm, and the dust optical depth is 0.5 at 10 μm. The dust optical properties of Justtanont & Tielens (1992) are used. The optical depth is scaled with the mass-loss rate for each star. The particular choices of the dust temperature law and optical depth play no role in our analysis, since our stars have relatively high mass-loss rates and the CO lines are dominantly excited through collisions. For example, changing the optical depth by a factor of 10 up or down leads to non-significant changes (≲1%) in the CO line intensities for a $\dot{M}_g = 2 \times 10^{-5}$ $M_\odot$ yr^{-1} and $v_\infty = 18$ km s^{-1} model (our median values, see below). The inner radius of the CO envelope is chosen to be 4×10^{14} cm. The resulting line intensities are not sensitive to this choice at the high mass-loss rates relevant for our sample.

The radiation fields considered in the excitation of the CO molecules are those of the star (assumed to be a blackbody at 2500 K and with a luminosity obtained from the SED fit), the dust (as calculated from the above dust temperature and optical depth), and the cosmic microwave background at 2.7 K. For the high mass-loss rates of our sample stars, collisional excitation dominates completely and these particular choices play no role.

We assume an initial fractional abundance of ^{12}CO/H$_2$, f_i, of 4×10^{-4}, which corresponds to about 80% complete formation of CO assuming solar abundances of C and O (see e.g. Agúndez et al. 2020). The abundance distribution of CO is eventually determined by photodissociation, in lines in the case of this species. We have used the recent results of Saberi et al. (2019) on circumstellar CO photodissociation to calculate the size of the CO envelope. The abundance distribution follows the law

$$f(r) = f_i \exp[-(\ln 2)(r/R_{1/2})^\alpha], \tag{4}$$

where $R_{1/2}$ and α are given by

$$R_{1/2} = 1.68 \times 10^{17} \left[\frac{\dot{M}_g}{10^{-5}} \right]^{0.57} \left[\frac{v_\infty}{15} \right]^{-0.35} \left[\frac{f_i}{4 \times 10^{-4}} \right]^{0.32} \text{[cm]}, \tag{5}$$

and

$$\alpha = 3.09 \left[\frac{\dot{M}_g}{10^{-5}} \right]^{0.09} \left[\frac{v_\infty}{15} \right]^{-0.13} \left[\frac{f_i}{4 \times 10^{-4}} \right]^{-0.04}, \tag{6}$$

respectively, where v_∞ is given in km s^{-1}, and $\dot{M}_g$ in $M_\odot$ yr^{-1}. These fits to the Saberi et al. (2019) results are appropriate for the mass-loss-rate, expansion velocity, and fractional abundances ranges relevant for this study. The same formulae have been used for ^{13}CO with the appropriate abundance. In general, the $J = 2–1$ and, in particular, the $J = 3–2$ model line emissions are relatively insensitive to the choice of $R_{1/2}$, discussed further in Sect. 6.5. The outer radius of the CSE is set to $3 \times R_{1/2}$.

The CO excitation analysis includes 82 rotational energy levels, up to $J = 40$ within the ground ($v = 0$) and first vibrationally excited ($v = 1$) states. Radiative transitions within and between the vibrational states and collisional transitions within the vibrational states are taken into account. The collisional rate coefficients between CO and para- and ortho-H$_2$ are taken from

Yang et al. ([2010](#)). An ortho-to-para-H_2 ratio of 3 was adopted for weighting the ortho-to-para-H_2 coefficients together. The rates cover 25 temperatures between 2 and 3000 K. The same ranges of transitions and rates are used for both CO isotopologues.

The best-fit circumstellar model for the ^{12}CO line emission is obtained by minimising the difference between the model and observational results in terms of the velocity-integrated flux densities by adjusting the only free parameters, the gas expansion velocity and the mass-loss rate. The estimate of the ^{13}CO fractional abundance is based on this model and the requirement that the model and the observational $^{12}CO/^{13}CO$ $J = 3–2$ velocity-integrated flux density ratios are the same. The ^{13}CO fractional abundance is the only free parameter in this case.

The availability of only two ^{12}CO lines (and their generally low S/N) and the use of the same circumstellar model for all stars make our mass-loss rate estimates particularly uncertain, at least by a factor of five. To this should be added the uncertainties due to the ^{12}CO abundance and the source distance. Likewise, the estimated $^{12}CO/^{13}CO$ abundance ratios are uncertain since they are based on only one ^{13}CO line. However, since this is a ratio estimate it has the advantage of being much less sensitive to the adopted circumstellar model than those of the mass-loss-rate. The ratio is also relatively insensitive to the adopted ^{12}CO abundance. A decrease/increase of the latter leads to an increase/decrease of the mass-loss rate and therefore a decrease/increase in also the estimated ^{13}CO abundance. In total, the uncertainty of the $^{12}CO/^{13}CO$ abundance ratio is about a factor of four.

In fact, there are indications that for most of our objects the adopted circumstellar model is not appropriate. Alternatively, the ^{12}CO line data have too low S/N. The signs of this are found in the ^{12}CO $J = 3–2/2–1$ line intensity ratios. In the models, this ratio depends sensitively on the mass-loss rate and to some extent on the kinetic temperature. Adopting our circumstellar model and $v_\infty = 18\,km\,s^{-1}$ we find that the $J = 3–2/2–1$ line intensity ratio goes from being >1 to becoming <1 as the mass-loss rate increases above $3 \times 10^{-5}\,M_\odot\,yr^{-1}$. At 10^{-6} and $10^{-4}\,M_\odot\,yr^{-1}$ the ratio is 1.5 and 0.6, respectively. A change of the kinetic temperature by -20% and $+20\%$, with respect to that given in Eq.([2](#)), leads to a mass-loss rate of 2×10^{-5} and $4 \times 10^{-5}\,M_\odot\,yr^{-1}$, respectively, at the crossing point, that is a relatively modest change. In the same way, a larger/smaller exponent (in absolute terms) in the kinetic temperature law leads to a cooler/warmer CSE and the crossing point moves to lower/higher mass-loss rates, but the effect is limited for reasonable changes. A comparison with the observational data is discussed in Sect. [6.4](#).

6. Results and discussion

For reasons to be explained in Sect. [6.3](#) we have divided our 22 objects into two groups: 17 objects are likely to be located within the inner GB, while five objects are likely to be lying in the foreground with unknown distances. The latter are discussed separately in Sect. [6.9](#).

6.1. Spectral energy distributions

A model SED has been fitted for all objects assuming isotropic dust density distributions following an r^{-2}-law, Sect. [5.1](#). The parameters of the best-fit models are given in Table [4](#), and all SEDs are shown in Fig. [4](#). It is apparent from the SEDs and the model fits that they can be divided into two distinct classes in terms of their appearance. For 16 sources the SED can be

**Table 4.** Results from the SED fits.

Source	A_{K_s} (mag)	$T_\star$ (K)	R_{in} (au)	$T_{d,in}$ (K)	$\tau_{9.7}$
Inner-GB objects:					
1 - OH358.083+0.137	1.51	3500	200	210	1.5
4 - OH358.505+0.330	0.98	4000	500	170	0.5
5 - OH359.140+1.137	0.56	5000	600	180	1.2
7 - OH359.220+0.163	2.16	3500	500	160	1.2
8 - OH359.233−1.876	0.42	3500	300	200	2.2
9 - OH359.467+1.029	0.71	2500	15	. . .	3.0
10 - OH359.543−1.775	0.32	5000	350	190	0.9
11 - OH359.664+0.636	1.10	2500	15	. . .	2.5
12 - OH359.745−0.404	1.89	2500	16	. . .	2.9
13 - OH359.805+0.200	1.80	2500	13	. . .	2.4
14 - OH359.826+0.153	2.04	2500	13	. . .	1.3
15 - OH359.902+0.061	2.08	2500	11	. . .	1.4
16 - OH0.173+0.211	1.62	2500	10	. . .	1.5
17 - OH0.221+0.168	1.54	2500	12	. . .	1.2
19 - OH0.739+0.411	1.40	2500	35	. . .	2.9
21 - OH1.221+0.294	1.92	2500	19	. . .	2.3
22 - OH1.628+0.617	0.84	2500	30	. . .	2.0
Foreground objects:					
2 - OH358.162+0.490	. . .	2500	14	. . .	2.5
3 - OH358.235+0.115	. . .	2500	12	. . .	1.1
6 - OH359.149−0.043	. . .	2500	13	. . .	1.7
18 - OH0.548−0.059	. . .	2500	14	. . .	1.7
20 - OH1.095−0.832	. . .	2500	14	. . .	2.6

Notes. The far-IR part and the ALMA points are not well fitted for many objects. See text for details on this.

fitted using a standard CSE of dust (hereafter SE), that is it is formed by a mass-loss rate constant with time. For the remaining six sources a detached dust CSE (hereafter DE), with an inner radius in the range 200–600 au, is required to fit the SED. The two objects with resolved source structure in the CO line data, OH358.505+0.330 and OH359.220+0.163, lie in this category. The classification of each object is given in Tables [5](#) and [6](#). Some aspects of the DE objects are discussed in more detail in Sect. [6.8](#).

It is noteworthy that the SEDs of the SE-type objects can all be well-fitted using a stellar (blackbody) temperature of 2500 K, a reasonable stellar effective temperature for a high-mass-loss-rate AGB star. However, the data put no strong constraints on this parameter. On the contrary, the SEDs of the DE-type objects are only well-fitted when a higher stellar temperature is used (this results in a better fit in the range 1 to 7 μm).

It is apparent that in the 13 objects where data at wavelengths longer than about 70 μm are available, the SED fits are often not very good. In eight objects (5 are SE objects, 3 are DE objects), the longer wavelength points are underestimated by a factor of a few, while they are severely underestimated in two objects (both are SE objects), OH0.548−0.059 and OH0.739+0.411. Increasing the outer radius by a factor of ten (i.e. 10^5 au, corresponding to a high-mass-loss-rate epoch of about 30 000 yr) leads to significantly improved, but not perfect, fits. Alternative ways of improving the fits are a mass-loss rate varying with time, a different dust CSE geometry, and/or different grain properties. However, the aim of this paper is not to provide the best possible fits to the long-wavelength regime of the SEDs by individually selecting the dust envelope geometry or dust composition for
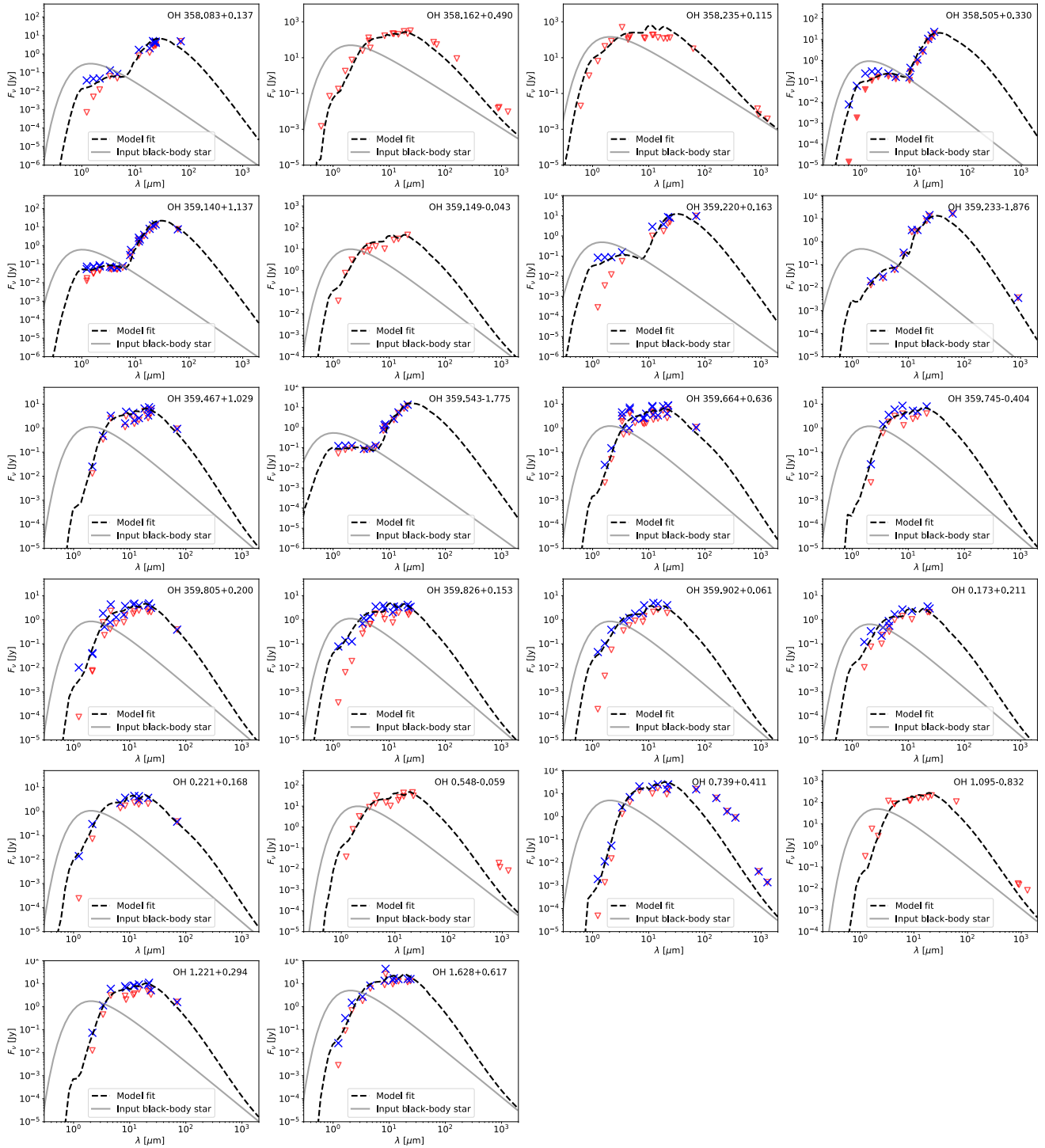
Fig. 4. SEDs composed of photometry data corrected (blue crosses) and not corrected (red triangles) for interstellar extinction. For the objects deemed to be foreground sources only the non-extinction-corrected data are shown. The best-fit model SED obtained from the radiative transfer calculations, input parameters given in Table 4, is given as a dashed, black line. The input stellar spectrum, approximated by a blackbody, is shown as the grey, solid line.

each source, but rather to put our CO line data in a broader context that is not dependent on the long-wavelength behaviour of the SED.

6.2. Stellar variability

Pulsation periods have been determined for 14 of our sample stars, Table 3. All but one, are long-period (in the range

500–1200^d), large-amplitude (a maximum to minimum ratio in the range $0.8 - 2.2$ magnitudes in the WISE W1 and W2 bands) pulsators, that is they have Mira-like variability. This agrees well with the results of Wood et al. (1998) for OH/IR stars in the GC, except the tail towards periods shorter than 500^d seen in the Wood et al. (1998) data. OH359.140+1.137 shows periodic variability, but with a very low amplitude (0.05^m and 0.1^m in the W1 and W2 bands, respectively), and hence cannot be classified

Table 5. Results for the inner-GB sources.

Source	SED type	$P^{(a)}$ (days)	$L^{(b)}$ ($L_\odot$)	$\dot{M}_g^{(c)}$ ($M_\odot\,\mathrm{yr}^{-1}$)	$R_{gd}^{(d)}$	$v_{sys}^{(e)}$ ($\mathrm{km\,s}^{-1}$)	$v_\infty^{(e)}$ ($\mathrm{km\,s}^{-1}$)	$^{12}\mathrm{CO}/^{13}\mathrm{CO}^{(f)}$
1 - OH358.083+0.137	DE	np	2100	2×10^{-5}	29	–24	22	5
4 - OH358.505+0.330	DE	np	6500	1×10^{-4}	125	–30	24	5
5 - OH359.140+1.137	DE	1000	6100	1×10^{-5}	8	–136	12	3
7 - OH359.220+0.163	DE	np	3400	8×10^{-5}	67	–137	16	7
8 - OH359.233−1.876	DE	np	3400	3×10^{-5}	20	–15	18	4
9 - OH359.467+1.029	SE	605	5600	2×10^{-5}	200	110	18	13
10 - OH359.543−1.775	DE	mp	5400	2×10^{-5}	12	90	36	2
11 - OH359.664+0.636	SE	550	6100	2×10^{-5}	250	–158	13	5
12 - OH359.745−0.404	SE	730	6000	1×10^{-5}	100	186	21	2
13 - OH359.805+0.200 [g]	SE	500	4300	5×10^{-6}	71	–51	21	4
14 - OH359.826+0.153	SE	500	5600	6×10^{-6}	171	–26	17	7
15 - OH359.902+0.061	SE	590	4300	1×10^{-5}	250	–133	19	4
16 - OH0.173+0.211 [g]	SE	512	3300	1×10^{-5}	333	52	18	. . .
17 - OH0.221+0.168	SE	663	5300	1×10^{-5}	200	64	23	10
19 - OH0.739+0.411	SE	570	25000	3×10^{-5}	176	–21	12	8
21 - OH1.221+0.294	SE	715	8700	7×10^{-5}	778	–261	13	50
22 - OH1.628+0.617	SE	830	25000	5×10^{-5}	250	–86	27	16

Notes. [a] The adopted period from Table 3 (np = non-periodic, mp = non-Mira multi-periodic variablity). [b] Obtained by integrating the fit to the extinction-corrected SEDs. [c] The uncertainty is estimated to be a factor of 5. [d] The gas-to-dust mass ratio estimated as $\dot{M}_g/\dot{M}_d$. The uncertainty is estimated to be a factor of seven. [e] Estimated as weighted averages of the results for the detected CO lines. The uncertainties are estimated to be $\pm$ 1.0 and $\pm$ 1.5 km s^{-1} for the systemic and expansion velocities, respectively. [f] The uncertainty is estimated to be a factor of 4. [g] Only the $^{12}\mathrm{CO}(J=2–1)$ line is used for the mass-loss-rate estimate.

Table 6. Results for the suspected foreground objects.

Source	SED type	$P^{(a)}$ (days)	$L^{(b)}$ ($L_\odot$)	D_L (kpc)	$\dot{M}_g^{(c)}$ ($M_\odot\,\mathrm{yr}^{-1}$)	$R_{gd}^{(d)}$	$v_{sys}^{(e)}$ ($\mathrm{km\,s}^{-1}$)	$v_\infty^{(e)}$ ($\mathrm{km\,s}^{-1}$)	$^{12}\mathrm{CO}/^{13}\mathrm{CO}^{(f)}$
2 - OH358.162+0.490	SE	1230	5600	1.2	1×10^{-5}	100	3	23	6
3 - OH358.235+0.115	SE	874	5600	0.7	3×10^{-7}	10	–21	19	8:
6 - OH359.149−0.043	SE	np	5600	2.8	. . .	. . .	48:	26:	. . .
18 - OH0.548−0.059	SE	np	5600	2.8	. . .	. . .	–48:	25:	. . .
20 - OH1.095−0.832	SE	sat	5600	1.2	3×10^{-6}	30	11	22	3

Notes. [a] The adopted period from Table 3 (np = non-periodic, sat = saturated data). [b] Assumed to be the same as the median value for the inner-GB sample. [c] The uncertainty is estimated to be a factor of 5. [d] The gas-to-dust mass ratio estimated as $\dot{M}_g/\dot{M}_d$. The uncertainty is estimated to be a factor of 7. [e] Estimated as weighted averages of the results for the detected CO lines. The uncertainties are estimated to be $\pm$ 1.0 and $\pm$ 1.5 km s^{-1} for the systemic and expansion velocities, respectively. A colon indicates an uncertain value. [f] The uncertainty is estimated to be a factor of four. A colon indicates an uncertain value.

as having Mira variability. The rest of the objects have either non-periodic (six objects; for these objects there are enough data to determine a periodicity if present) or non-Mira multi-periodic variability (one object), or the object is so bright that the fluxes are saturated (one object).

There is a clear difference between the SE and DE sources in terms of their variability. Among the 16 SE sources, 13 show Mira-like variability, two are non-periodic, and for one the fluxes are saturated. On the contrary, for the six DE sources four are non-periodic, one shows only low-amplitude variability, and one shows multi-period, non-Mira-like variability.

6.3. Luminosities

We have found that 17 objects have luminosities, obtained by integrating the fit to the extinction-corrected SED for each

source, consistent with them being AGB stars if placed at our adopted distance of the GC, 8.2 kpc. Eleven of these objects have systemic velocities (in the local standard of rest frame) in the range $|v_{sys}| > 50\,\mathrm{km\,s}^{-1}$, further strengthening their association with the inner GB, where radial systemic velocities can be high also at a line-of-sight direction close to $\ell = 0°$. When looked at separately in terms of their luminosities and mass-loss-rate characteristics, there is nothing that distinguishes the remaining six stars (with $|v_{sys}| < 50\,\mathrm{km\,s}^{-1}$) from the 'higher-velocity' stars. Therefore, these 17 stars form our sub-sample of inner-GB OH/IR stars, see Table 5. About two-thirds of them are SE sources and one third DE sources. Only three of the inner-GB objects are detected in 324 GHz continuum.

Two of the inner-GB objects, OH0.739+0.411 and OH1.628+0.617, have markedly higher luminosities than the others, $\approx 25\,000\,L_\odot$, and they are among the three objects in
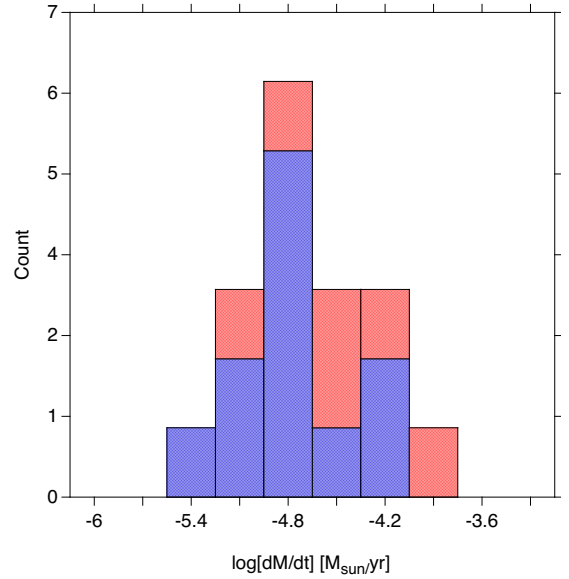
Fig. 5. Luminosity distribution of the inner-GB sample (blue for SE objects, red for DE objects).
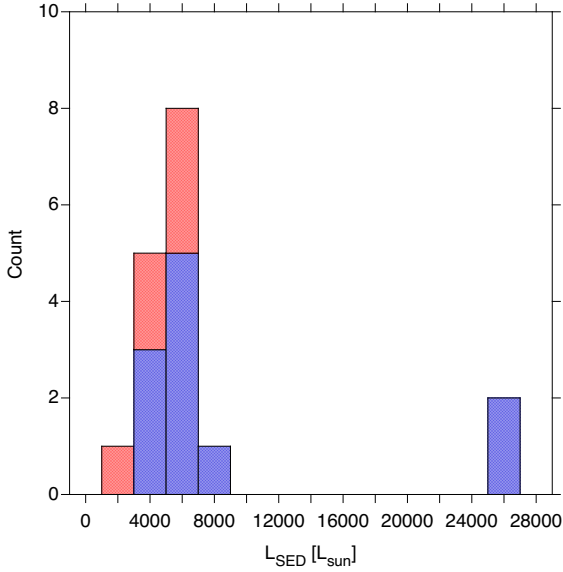
Fig. 6. Gas mass-loss rate distribution of the inner-GB sample (blue for SE objects, red for DE objects).

this sub-sample that are detected in 324 GHz continuum. Except for this, they seem not to be different from the inner-GB objects. Therefore, we retain them in this sub-sample, but note that there is a strong possibility that they are instead foreground objects.

This leaves five objects out of the original 22 sources, all of them SE sources, for which the estimated luminosities become higher than expected for an AGB star if placed at the distance of the GC, for three of them even higher than expected for a red supergiant. Most likely these are foreground AGB stars, and they will be discussed separately in Sect. 6.9. All of them are detected in 324 GHz continuum.

Figure 5 shows the luminosity distribution for our inner-GB sample. The median luminosity is $5600\,L_\odot$ and the range covered is 2100–$8700\,L_\odot$ for the majority of the objects. There are two outliers at a higher luminosity, $25\,000\,L_\odot$. In this sense, our objects appear in many respects similar to the sources in the GB discussed by van der Veen & Habing (1990) and also by Groenewegen & Blommaert (2005), Jiménez-Esteban & Engels (2015), and Blommaert et al. (2018), for instance. Using the results of Karakas (2014), the median luminosity translates into an initial mass of $\approx 1.2\,M_\odot$ if the star has solar metallicity and lies at the peak of the AGB (using the results of Ventura et al. 2018 gives the same result)[4]. This means that these objects will not become carbon stars, and their masses fall well below the limit for the hot-bottom-burning (HBB) process. Using instead the often used, but older, results of Vassiliadis & Wood (1993) and the same assumptions, the median luminosity translates into an initial mass of $\approx 1.6\,M_\odot$, still well below the HBB mass limit. The initial mass estimates translates to an age in the range 4–7 Gyr for these sources. For the two higher-luminosity stars, $25\,000\,L_\odot$ indicates an initial mass of about $4.3\,M_\odot$ if at solar metallicity and at the peak of the AGB (Karakas 2014). That is, these are much younger stars (about 0.3 Gyr) that may have started HBB. Such stars were also found by Groenewegen & Blommaert

---

[4] The metallicity of the Bulge is a complicated issue. There exists sub-solar, solar, and super-solar metallicity populations (see e.g. García Pérez et al. 2018). However, the initial mass estimate is relatively independent of metallicity. Following Karakas (2014) we find that a metallicity of $Z = 0.007$ results in $M_i \approx 1\,M_\odot$, while $Z = 0.03$ results in $M_i \approx 1.4\,M_\odot$.
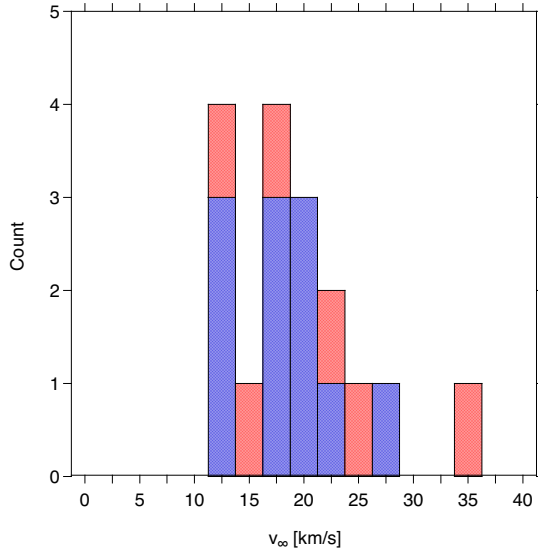
(2005) towards the GC. Alternatively, they may be foreground stars.

We have compared our estimated luminosities with those obtained from the pulsational periods using different period-luminosity (PL) relations. Whitelock et al. (1991) derived a PL relation using a mixture of Galactic and Large Magellanic Cloud objects of O-type with periods in the range 120–2000^d (≈ 40 objects; $M_{\mathrm{bol}} = -2.55 \log P + 1.85$ mag). For the eleven inner-GB objects with determined Mira-like variability, this relation gives luminosities that are, on average, two times higher than our results. Groenewegen et al. (2020) used Magellanic Clouds objects of O-type with periods in excess of 1000^d (11 objects; $M_{\mathrm{bol}} = -2.97 \log P + 2.59$ mag). In comparison, this relation gives luminosities that are, on average, three times higher than our results. Clearly our objects lie below these PL relations. A similar conclusion was reached by Wood et al. (1998) and Blommaert et al. (1998) for their samples of OH/IR stars. Wood et al. (1998) argued that this is an effect of lengthened periods due to extensive mass loss (and hence lower present stellar masses), possibly strengthened by metallicity effects. The only exceptions are the $25\,000\,L_\odot$ objects. The luminosities obtained from the Whitelock et al. (1991) relation and their pulsational periods are two times lower than our results. This may be a strong indication that these are actually foreground stars.

6.4. Mass-loss rates and gas kinematics

The gas-mass-loss rates and terminal gas-expansion velocities have been estimated using a radiative transfer code and the ^{12}CO $J = 2$–1 and 3–2 lines. The results are summarised in Table 5. The gas-mass-loss-rate distribution for the 17 stars in the inner-GB sample, see Fig. 6, has median of $2 \times 10^{-5}\,M_\odot\,\mathrm{yr}^{-1}$. This means that this is definitely a high-mass-loss-rate sample compared with, for instance, a solar neighbourhood sample of O-type AGB stars with a median mass-loss rate of $3 \times 10^{-7}\,M_\odot\,\mathrm{yr}^{-1}$ (the results of Olofsson et al. 2002 and González Delgado et al. 2003 as summarised by Ramstedt et al. 2009). In terms of mass-loss characteristics, the inner-GB sub-sample stars are similar to nearby Miras like GX Mon, IK Tau, and WX Psc, whose masses are estimated to lie in the range 1.1–$1.5\,M_\odot$

Fig. 7. Terminal gas expansion velocity distribution of the inner-GB sample (blue for SE objects, red for DE objects).

Fig. 8. Flux densities of the ^{12}CO($J=2$–1) and OH 1612 MHz lines plotted versus each other for the inner-GB sample.

(De Nutte et al. 2017; Danilovich et al. 2017). Jiménez-Esteban & Engels (2015) and Blommaert et al. (2018) derived mass-loss rates for their samples of stars similar to ours by solving the momentum equations for gas and dust (coupled via friction) and obtained mass-loss rates that are a factor of a few higher than ours, but this way of estimating mass-loss rates is not without its problems (Ramstedt et al. 2008).

The terminal gas-expansion velocity distribution of our inner-GB sources, see Fig. 7, has a median of $18\,\mathrm{km\,s^{-1}}$. This result can be compared with the peaks of the velocity distributions of OH/IR stars in the Galactic Plane ($12\,\mathrm{km\,s^{-1}}$), the GB ($14\,\mathrm{km\,s^{-1}}$), and the GC ($19\,\mathrm{km\,s^{-1}}$; Sjouwerman et al. 1998), and the median of $7\,\mathrm{km\,s^{-1}}$ for a solar neighbourhood sample (Ramstedt et al. 2009). It has been argued that higher-velocity sources are drawn from a younger population than the lower-velocity sources (Lindqvist et al. 1992a), but it could also be an effect of our stars reaching the tip of the AGB and the end of their the mass-loss evolution, since, in general, mass-loss rate and expansion velocity are positively correlated (Höfner & Olofsson 2018). We find no such correlation for our inner-GB sub-sample, but this is most likely due to the limited range measured for, and the relatively large uncertainties in the estimates of, both these quantities. Nevertheless, our objects fall in the correct regime of this correlation. Finally, observations of OH 1612 MHz masers and CO line emission towards AGB stars in the Large Magellanic Cloud suggest that the gas expansion velocities are lower at lower metallicity (Goldman et al. 2017; Groenewegen et al. 2016). Hence, the high expansion velocities of our inner-GB sample sources suggest that they are not low-metallicity objects.

As discussed in Sect. 5.2 the ^{12}CO $J=3$–2/2–1 line intensity ratio depends sensitively on the mass-loss rate, and to a lesser degree on the kinetic temperature. We find a significant discrepancy, by factors of 1.5–3, between the observational and model ratios (for the derived mass-loss rate) in eleven of our inner-GB sources, and under-estimates are as common as over-estimates. The most likely explanation is a mixture of an inadequate circumstellar model and an inadequate S/N of the observational data. Higher quality data on more ^{12}CO line transitions are required in order to address this issue.

The angular sizes (in diameter) corresponding to the $R_{1/2}$ values, as calculated using Eq. (5), for our inner-GB sources lie in
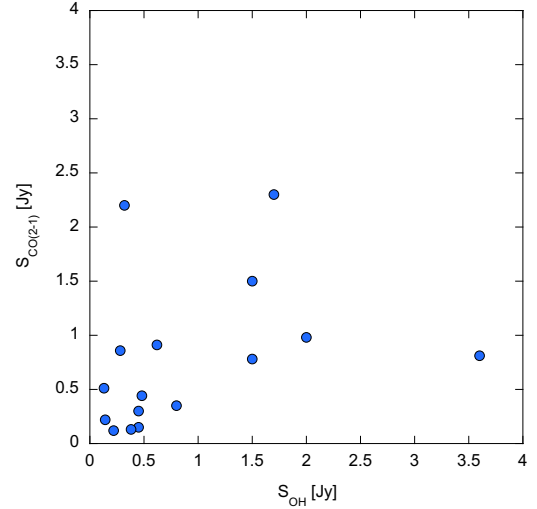
the range $1.''6$–$8.''4$. Since the MRSs are about $2.5''$ and $1''$ for the $J=2$–1 and 3–2 lines, respectively, there is a risk that we lose flux. We have made a crude estimate for a $\dot{M}_\mathrm{g}=10^{-4}\,M_\odot\,\mathrm{yr}^{-1}$ and $v_\infty=20\,\mathrm{km\,s^{-1}}$ model source at a distance of 8.2 kpc. In this rather extreme case, the $R_{1/2}$ value corresponds to $8.''6$ in diameter. When observed with beam sizes that equal the MRSs, about 60% and 50% of the total flux densities are lost in the $J=2$–1 and 3–2 lines, respectively. For our median values of $2\times10^{-5}\,M_\odot\,\mathrm{yr}^{-1}$ and $18\,\mathrm{km\,s^{-1}}$ the loss is much less, about 14% in both lines. This means, that, on average, the estimated mass-loss rates are not significantly affected by any missing flux, only at the extreme upper end, the underestimate may be about a factor of two. The effect becomes less if the $R_{1/2}$ values are smaller than predicted by Eq. (5), see discussion below.

Both the CO and OH 1612 MHz line intensities are expected to depend on the mass-loss rate (Baud & Habing 1983; Ramstedt et al. 2008). We plot the ^{12}CO $J=2$–1 flux density versus that of the OH 1612 MHz line for the inner-GB sample in Fig. 8. As expected, there is a correlation, but it is not particularly tight. This is most likely due to the OH line being a significantly poorer mass-loss-rate estimator than the CO line. Nevertheless, it shows that the strength of the OH 1612 MHz line can be used, as a first approximation, to estimate the expected strengths of the CO rotational lines.

6.5. CO photodissociation and brightness distributions

We have used the results of Saberi et al. (2019) to calculate the photodissociation radii of ^{12}CO and ^{13}CO, $R_{1/2}$, for each source as outlined in Sect. 5.2. These are based on the assumption of an interstellar UV radiation field with a strength applicable to the solar neighbourhood. It is possible, even very likely, that this radiation field is considerably stronger in the region of the GC. This will decrease the CO photodissociation radius, although the effect is relatively moderate for higher-mass-loss-rate objects. An increase by a factor of four in the strength of the UV radiation field leads to a decrease in $R_{1/2}$ for ^{12}CO by only 30% for a $2\times10^{-5}\,M_\odot\,\mathrm{yr}^{-1}$ and $15\,\mathrm{km\,s^{-1}}$ object, and even less for higher mass-loss rates, as shown by Saberi et al. (2019).

Nevertheless, this opens up the question of how much the uncertainty in the CO photodissociation radius will affect our estimated mass-loss rates. Decreasing $R_{1/2}$ by a factor of three for

a model with our median values, $2 \times 10^{-5}\ M_\odot\ \mathrm{yr}^{-1}$ and $18\ \mathrm{km\,s}^{-1}$, results in flux densities lowered by 34% and 6% for the ^{12}CO $J = 2$–1 and 3–2 lines, respectively. This corresponds to a mass-loss rate under-estimated by about 20%, well within the uncertainty of this estimate. Consequently, the UV radiation field in the inner GB must be substantially higher than that in the solar neighbourhood to have any effect on our estimated mass-loss rates.

Our estimated source sizes are (deconvolved) FWHMs of Gaussian fits to the velocity-integrated brightness distributions (the θ_s results are summarised in Tables A.1–A.3), and the question is if they contain any useful physical information, for instance, on the photodissociation radii. We have used our radiative transfer model to test this for the ^{12}CO(2–1) line, since this has the most extended brightness distribution and should consequently be the most-affected one of our observed lines. The adopted models all have $v_\infty = 18\ \mathrm{km\,s}^{-1}$, and we use three mass-loss rates, 4×10^{-6}, 2×10^{-5}, and $1 \times 10^{-4}\ M_\odot\ \mathrm{yr}^{-1}$ (this covers well the mass-loss-rate range of our inner-GB sub-sample). The distance is 8.2 kpc and the beam size is $0\rlap{.}''19$. The result is that for these conditions, the θ_s values of the velocity-integrated model brightness distributions are essentially independent of the photodissociation radius. The latter has to be decreased by a factor of ten to give a noticeable result on θ_s, a decrease by 40%. Thus, we can conclude that our estimated source sizes, in all likelihood, give no information on the photodissociation radius. Relations between Gaussian fits to brightness distributions and photodissociation radii of nearby, lower-mass-loss-rate sources are discussed in Ramstedt et al. (2020).

Finally, we test whether or not our radiative transfer modelling is able to reproduce the observed brightness distributions. In Fig. 9, we compare the azimuthally averaged observed brightness distributions of the ^{12}CO(2–1) line towards four of our sources (these are inner-GB objects having the largest θ_s and the highest S/N data), with the brightness distributions of the best-fit radiative transfer models for each source (obtained with a Gaussian beam having a FWHM that equals that of the synthesised beam). As can be seen, the narrow and bright central peak of the observed brightness distributions are well reproduced in the models. On the contrary, the observed extended low-surface-brightness emission in the observational data is clearly under-estimated in the models. Within the adopted circumstellar model, the only way to selectively increase the model brightness in the external parts is to raise the minimum kinetic temperature, $T_{\min}$ (it should be noted here that the physical properties of the external parts of AGB CSEs are particularly poorly constrained). However, in order to still fit the observed velocity-integrated intensities, this requires a corresponding decrease in the mass-loss rate, to the extent that the under-estimate of the brightness in the external parts persists. Hence, the only way to get a better fit to the observed brightness distribution is to modify the circumstellar model, such as the geometry, or allow a deviation from an r^{-2}-law for the density distribution.

There are also suggestions of modulations in the brightness distributions that can be due to ring-, arc- or spiral-like structures in the density distribution. Clearly, a study of structure in the CSEs requires higher S/N data and larger MRSs than provided by our data set.

6.6. Gas-to-dust mass ratios

Our estimate of the gas-to-dust mass ratio, R_{gd}, is obtained as $\dot{M}_{\mathrm{g}}/\dot{M}_{\mathrm{d}}$, and the results for the inner-GB objects are summarised
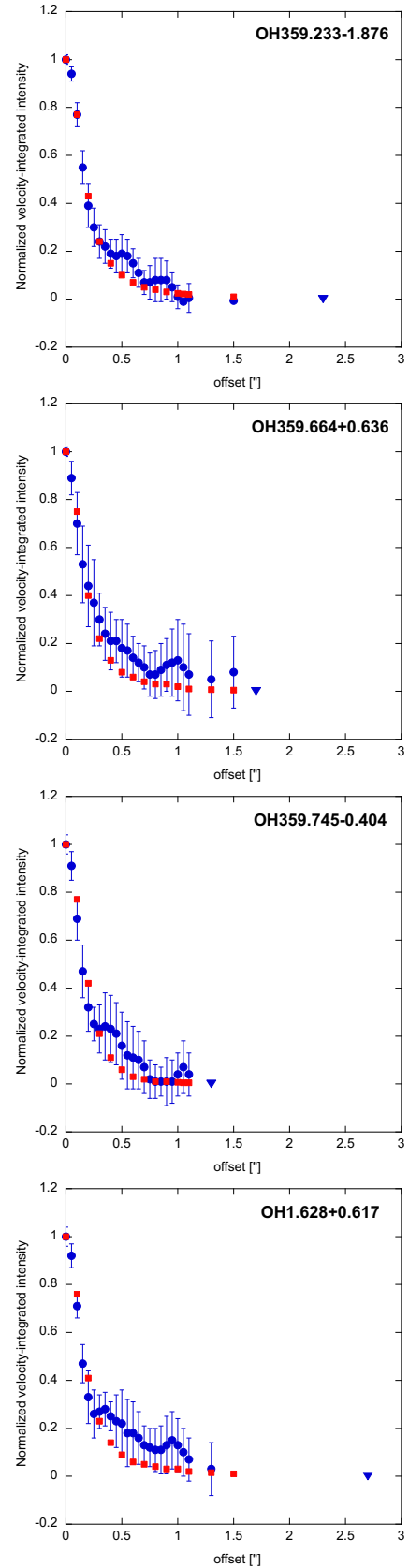
Fig. 9. Azimuthally averaged observed brightness distributions of the ^{12}CO(2–1) line towards four objects (blue filled circles), normalised intensity scales. The error bars are $\pm 1\sigma$. The blue triangle gives the photodissociation radius in angular units, $R_{1/2}/D$. The red squares shows the brightness distribution of the best-fit radiative transfer model for each source obtained with a beam that equals the synthesised beam.
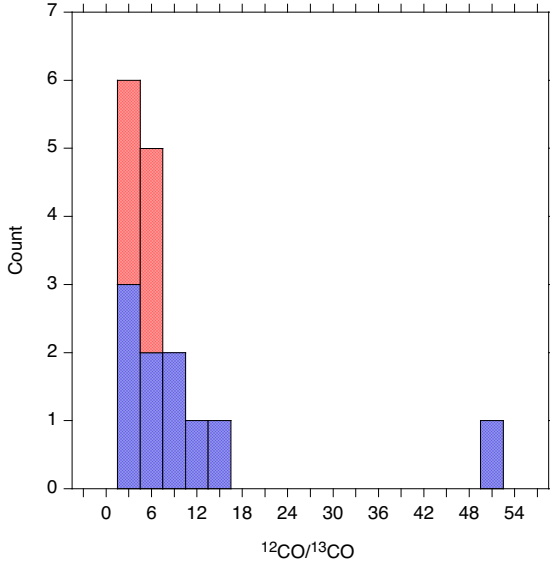
Fig. 10. Circumstellar ^{12}CO/^{13}CO abundance ratio distribution for the inner-GB sample (blue for SE objects, red for DE objects).

in Table 5. It is clear that we must separate the discussions of the SE and DE objects. For the SE sources the resulting R_{gd} values range from about 70 to 780 with a median of 200. This is in the range found for other O-type AGB stars (e.g. Ramstedt et al. 2008, and references therein). On the contrary, for the DE sources the R_{gd} values are much lower, in the range 5–143. This is further discussed in Sect. 6.8.

6.7. The circumstellar ^{12}CO/^{13}CO abundance ratio

The circumstellar ^{12}CO/^{13}CO abundance ratio has been estimated through a radiative transfer analysis, in order to correct for any optical depth effects, of a single ^{13}CO line within the circumstellar model determined from the ^{12}CO lines. As such, it is associated with some considerable uncertainty, at least a factor of four as discussed in Sect. 5.2. The results are summarised in Table 5 and presented in Fig. 10. For the inner-GB objects the ^{12}CO/^{13}CO abundance ratios range from 1.6 to 16 (with an outlier at 50) with a median of 5.

The circumstellar ^{12}CO/^{13}CO abundance ratio is of particular interest if it is a good measure of the stellar ^{12}C/^{13}C isotope ratio. There are good reasons to believe that this is the case. The two main processes that can alter the molecular ratio are isotope-selective chemistry and photodissociation. The processes determining the initial ^{12}CO/^{13}CO abundance ratio are in all likelihood not isotope-selective. Further out in the CSE, the photodissociation is isotope-selective since it occurs in lines and the optical depth is lower for the ^{13}CO lines than the corresponding ^{12}CO lines. However, this can be counter-acted by the exchange reaction that favours the formation of ^{13}CO at the expense of ^{12}CO in low-temperature gas (Watson et al. 1976). These CSE processes have been studied in detail by Saberi et al. (2019, 2020), and the conclusion is that the circumstellar ^{12}CO/^{13}CO abundance ratio in the external part of the CSE of a high-mass-loss-rate object is only slightly above the initial ^{12}CO/^{13}CO value, which is determined by the stellar ^{12}C/^{13}C isotope ratio. This means that, if anything, we overestimate the latter. Saberi et al. (2020) also tested the effect of a higher UV radiation field. It will lead to a further slight increase in the circumstellar ^{12}CO/^{13}CO abundance ratio in the external parts of

the CSE, but the effect is marginal for the mass-loss rates of our objects.

The very low stellar ^{12}C/^{13}C isotope ratios inferred in this way are theoretically problematic, since the stars in our inner-GB sample are relatively low-mass stars (1.2–1.4 $M_\odot$) that do not go through HBB. The latter is the only viable nucleo-synthetic way of producing very low ^{12}C/^{13}C isotope ratios, close to the equilibrium value of the CNO-cycle $\approx$3.5, but it requires a stellar mass in excess of 4 $M_\odot$ (Karakas & Lugaro 2016). In the case of lower-mass stars this isotope ratio is set by the first dredge-up during red giant branch (RGB) evolution, and it is difficult, in theory, to obtain isotope ratios below 20 (Karakas & Lugaro 2016), unless there is some efficient extra mixing such as thermohaline mixing, which is introduced through a parameterised approach (see Karakas & Lattanzio 2014 for a discussion of different mixing processes).

Our result should be put into the context of results for other O-type red giants. Ramstedt & Olofsson (2014) found circumstellar ^{12}CO/^{13}CO abundance ratios that range from 6 to 66 with a median of 13 in their sample of solar neighbourhood, most likely lower-mass, mass-losing, O-type AGB stars. For the high-mass-loss-rate objects GX Mon, IK Tau, and WX Psc, with estimated masses in the range 1.0–1.5 $M_\odot$ (see above), the results are 11, 10, and 13, respectively. For their remaining ten sources with mass-loss rates in excess of 5×10^{-6} $M_\odot$ yr^{-1}, but without mass estimates, the median value is 15. The work of Hinkle et al. (2016), based on stellar atmosphere synthetic spectra of O-type AGB stars (mainly Miras with weak, if any, mass loss), emphasises these results: they found a median stellar ^{12}C/^{13}C of 17, and no source with a reliable ratio lower than 10 in their sample of 33 stars. Results for O-type giants on the RGB has also been obtained. Gilroy (1989) estimated stellar ^{12}C/^{13}C isotopic ratios in the range 6–17 for stars in open clusters and masses in the range 1–2 $M_\odot$. Gilroy & Brown (1991) found an average ^{12}C/^{13}C of 13 for stars at the tip of the RGB and at the Horizontal Branch in the open cluster M67. Tsuji (2007) found stellar ^{12}C/^{13}C isotopic ratios in the range 8–16 for a sample of eight RGB stars. Considering the uncertainties of our estimates, it is currently not possible to judge whether or not the stars in our sample have significantly lower inferred stellar ^{12}C/^{13}C isotope ratios than those estimated by others for RGB and AGB stars. On the other hand, there is no obvious reason why our analysis should lead to a systematic under-estimate of the ^{12}CO/^{13}CO abundance ratio by factors of two to three. Finally, we note here that Delfosse et al. (1997) also estimated very low circumstellar ^{12}CO/^{13}CO abundance ratios for a small sample of OH/IR stars, and that Justtanont et al. (2015) inferred high ^{17}O/^{18}O isotope ratios for a sample of five OH/IR stars. The latter result strongly suggest HBB processing. The masses of the stars in these two studies are not known, but they, most likely, belong to a population of higher-mass AGB stars.

6.8. Objects with detached dust CSEs

About a third of our inner-GB objects belongs to a distinct class of sources where the SEDs indicate that the dust CSEs are detached from the central source, that is their mass loss has ceased some time ago, the DE objects, see Fig. 4. The fits to their SEDs also suggest that their central stars are warmer. These objects are non-periodic, or, in one case (OH359.140+1.137), show non-Mira-like variability of very low amplitude. These characteristics strongly indicate that the DE objects are the most evolved in our total sample, that is they lie close to the tip of the AGB, and in some cases may even have left the AGB. The two

sources with resolved structure in the CO line brightness distributions are both of the DE type, and they are probably the objects that are most evolved. As a guideline the maximum estimated inner radius, 600 au, corresponds to a time scale of ≈ 150 yr for an expansion velocity of $20\,\mathrm{km\,s^{-1}}$. It may be that our way of selecting the sample has led to a bias towards objects with DE characteristics, but it is difficult to quantify the magnitude of any bias, if present.

Unfortunately, our sample is too small to allow a detailed comparison of the circumstellar characteristics of the SE and DE sources. This can only be done by increasing the sample size and by observing emission from more ^{12}CO and ^{13}CO transitions. For illustration, we have separated the SE and DE objects in the figures presenting the luminosity, mass-loss rate, expansion velocity, and ^{12}CO/^{13}CO distributions.

The estimated gas-to-dust-mass ratios warrants a discussion, however. For the DE sources we find a range in R_{gd} from 5 to 143, and a median of 36. These are low values, and a possible explanation is that the SED fits give erroneous results for $\dot{M}_{\mathrm{d}}$. Furthermore, the dust temperatures at the inner radii of the dust CSEs are remarkably similar for all the DE sources, 185 ± 25 K. The fact that the SEDs of all the DE objects peak at the same wavelength, $\approx 25\,\mu$m, is in line with this. In the context of the adopted model, an isotropic dust density distribution with different inner radii, this is difficult to understand. This opens up the question of an alternative, non-isotropic, dust density distribution for the DE sources as, for instance, suggested by Decin et al. (2019) for evolved OH/IR stars. This can be analysed along the lines of Wiegert et al. (2020), but it would lead too far to test this out in detail in this paper. The conclusion for now is that there is no obvious way to produce the amount of emission we see with significantly less dust, and hence increase the R_{gd}. The main argument is that the optically thin part of the dust emission spectrum starting at about $30\,\mu$m to longer wavelengths needs a certain amount of dust at relatively low temperatures. There could be warmer dust contributing at those wavelengths but that would have to be hidden by high optical depths at shorter wavelengths.

Finally, we note here that the estimated inner radii of the dust CSEs of the DE sources are small enough that they will not affect the intensities of the CO lines discussed in this paper. Our radiative transfer calculations show that the intensities of the CO lines are not affected by increasing the inner radius of the CO envelope to, for instance, 600 au. For OH, the situation is different. Using the results of Netzer & Knapp (1987) we estimate that the radius of the OH shell is ≈ 2000 au for a mass-loss rate of $2 \times 10^{-5}\,M_{\odot}\,\mathrm{yr^{-1}}$ and an expansion velocity of $18\,\mathrm{km\,s^{-1}}$ (our median values). However, if the interstellar UV radiation field is stronger in the inner GB than in the solar neighbourhood, this would lead to smaller molecular envelopes. As discussed in Sect. 6.5, the CO photodissociation radii of the inner-GB subsample sources cannot be estimated from our data. In fact, they could be substantially smaller without affecting the observed source sizes and the estimated mass-loss rates. Since the H_2O and OH molecules are photodissociated in the continuum, and not in lines as CO (see van Dishoeck 1988 for a description of photodissociation in continuum and in lines), the size of the OH shell is more affected by an increased UV radiation field than is the CO envelope. An OH shell about three times smaller than that obtained for a solar neighbourhood UV radiation field, that is about 700 au for our median values of mass-loss rate and expansion velocity, fits very well a scenario where sources with CSE inner radii in excess of ≈ 700 au would not be detectable as OH/IR stars, and hence not end up in our sample.

6.9. Suspected foreground objects

For five of our sample objects the luminosities obtained, if placed at our adopted distance to the GC, lie at the maximum luminosity of an AGB star ($\approx 50\,000\,L_{\odot}$) or considerably higher. These objects are therefore in all likelihood foreground objects, Table 6. They all belong to the SE class. Periods have been determined for two, two are non-periodic, and for the remaining star the photometry fluxes are saturated. All five objects are detected in 324 GHz continuum. For these objects, the SEDs shown in Fig. 4 are not extinction-corrected. It should be noted that neither of these sources, nor any other sources in our total sample, have a useful parallax in *Gaia* EDR3 (Gaia Collaboration 2021).

Two objects, OH358.162+0.490 and OH1.095−0.832, are the, by far, strongest emitters in the ^{12}CO($J = 2$–1) line in our total sample, Table A.1. The CO line profiles have high S/N, and have the characteristics expected of a thermal (i.e. not masing) line from an AGB CSE, Figs. 3, A.5, and A.6. The brightness distributions are centrally peaked and resolved. The latter is reflected in the ^{13}CO($J = 3$–2) line profiles which are double-peaked as expected for circumstellar, optically thin, resolved line emission. Their OH 1612 MHz lines are the, by far, strongest in our total sample, and their line profiles are the characteristic double-peaked ones (Sevenster et al. 1997). Their systemic and terminal gas expansion velocities are 3 and 11 km s^{-1} and 23 and 22 km s^{-1}, respectively, as determined from our CO data. They are also the two strongest 324 GHz continuum sources in our total sample. Both coincide with strong IRAC sources, Fig. A.4. OH358.162+0.490 show long-period Mira-like variability, while for OH1.095−0.832 the photometry data are saturated. These objects show all the characteristics of being AGB stars.

In the case of OH358.235+0.115, the CO line data have relatively low S/N, Fig. A.1, but the emissions are centrally peaked and coincide with a strong 5.8 μm IRAC source, Fig. A.4. The OH 1612 MHz line shape is not the characteristic one, being triple-peaked rather than double-peaked and having no sharp outer edges (Sevenster et al. 1997). The systemic and gas expansion velocities estimated from the CO and OH data differ, the results from the CO data are −21 and 19 km s^{-1}, respectively. The object is relatively strong in 324 GHz continuum. The variability is periodic, so this object is most likely an AGB star despite the strange OH line profile.

OH359.149−0.043 exhibits very strange brightness distributions in all three CO lines in the form of arc-like structures extending about 2″.5, Fig. A.1. Nevertheless, the emission lies in the vicinity of a strong 8 μm IRAC source, Fig. A.4. The CO line shapes appear reasonable from a circumstellar perspective (Figs. 3, A.5, and A.6), although the ^{13}CO($J = 3$–2) line is somewhat sharply peaked, but there is a problem with interstellar CO line emission that cannot be removed by eliminating short-baseline data without losing flux in the circumstellar CO lines. The OH 1612 MHz line shape is double-peaked, but narrow (covering about 15 km s^{-1}) and not apparently of the characteristic type (Sevenster et al. 1997). The CO data suggest a considerably higher gas expansion velocity, 26 km s^{-1}. A weak continuum source at 324 GHz is detected at the position of the near-IR source. This is tentatively an AGB star, but the structures in the CO line brightness distributions suggest that its circumstellar characteristics are not of the normal type, so we refrain from modelling the CO line emission.

OH0.548−0.059 is also an object with strange characteristics. The CO line brightness distributions are centrally peaked,

Fig. A.1, just about resolved, and they coincide with a strong 5.8 µm IRAC source, Fig. A.4. The CO line profiles are more difficult to interpret. The ^{13}CO($J = 3$–2) line is broad (covering about 90 km s^{-1}) and covers the same velocity range as the OH 1612 MHz line (Fig. 3), although the OH data are of limited quality and the double-peak structure is not obvious (Lindqvist et al. 1992b). Unfortunately, the ^{12}CO line spectra are of very low quality (Figs. A.5 and A.6), mainly due to the problem with interstellar CO line emission along the line of sight, and they do not provide any insight into the circumstellar characteristics. The ALMA continuum fluxes lie high above the fit to the SED, Fig. 4. Also in this case we refrain from modelling the CO line emission.

The most reasonable assumption is that the three objects for which we attempt a CO line modelling are of the same character as our inner-GB objects, that is they have a luminosity of 5600 $L_\odot$, but lie closer to us. We note that for the two objects with determined periods, this luminosity lies well below those obtained from PL relations (see Sect. 6.3 for a discussion on this). Using a luminosity of 5600 $L_\odot$ and the non-extinction-corrected SEDs, we derive the distances D_L (the same approach is used for the remaining two sources), see Table 6. They lie in the range 0.7 to 1.2 kpc. This may indicate that the distances are under-estimated, since it is more likely that the sources are spread out over the distance to the GC. Their systemic velocities are within the $|v_{sys}| \lesssim 20$ km s^{-1} range.

We have derived their circumstellar characteristics using the D_L distance. For OH358.162+0.490 and OH1.095−0.832 the gas mass-loss rates lie 2 and 7 times, respectively, below the median for the inner-GB sample. For OH358.235+0.115 the gas mass-loss rate is as low as 3×10^{-7} $M_\odot$ yr^{-1}, much lower than expected for a proper OH/IR star, suggesting that either the circumstellar model is wrong for this object, or its distance is substantially larger. In fact, its R_{gd} is as low as 10 suggesting that something is wrong. For the two other objects the R_{gd} values are 30 and 100, also low compared to the inner-GB sample. We note that the R_{gd} estimates are, to a first approximation, distance-independent (the necessity to apply extinction correction will change this). The ^{12}CO/^{13}CO ratios are 6 and 3 for OH358.162+0.490 and OH1.095−0.832, respectively, in line with the results for the inner-GB objects. The corresponding result for OH358.235+0.115, 8, must be considered very uncertain.

Finally, the three objects that we consider to be firmly established AGB stars among the foreground objects are the only objects in our full sample in which we detect also the H^{13}CN($J = 4$–3) line, Table A.4 and Fig. A.7. Despite being a C-bearing species, hydrogen cyanide (HCN) is ubiquitously detected also towards O-type AGB stars (Schöier et al. 2013). However, its circumstellar abundance is down by more than two orders of magnitude compared to that estimated in C-type objects (Schöier et al. 2013). Consequently, the HCN rotational lines in O-type objects are considerably weaker than the CO rotational lines, for instance, in the range 10–20% for the HCN($J = 4$–3)/CO($J = 3$–2) intensity ratio (Schöier et al. 2013; Ramstedt & Olofsson 2014). Therefore, our detections of the rarer isotopologue, H^{13}CN, were done at surprisingly high intensity levels, about 10–30% of that of the ^{12}CO($J = 3$–2) lines. Thus, this result further strengthen the conclusion that our sources are rich in ^{13}C. We note here that, as opposed to the case of CO, HCN is photodissociated in the continuum and hence we do not expect any effects of circumstellar isotope-selective processes (Saberi et al. 2020).

7. Conclusions

Observing OH/IR stars in CO line radiation towards regions of high extinction is a difficult task due to the contamination of ubiquitous interstellar CO along the line of sight. At the distance of the GC this is further exacerbated by the weakness of the circumstellar line and continuum radiation. Nevertheless, through the use of the ALMA interferometer both of these problems have been, at least partly, circumvented, and with observations of two rotational lines of ^{12}CO, one of ^{13}CO, and mm-wave continuum emission, we can infer interesting characteristics of a sample of 22 OH/IR stars in directions within 2° of the GC, the inner GB. All objects are detected in at least one CO line, and eight of them are detected in 324 GHz continuum. The CO line brightness distributions coincide with infrared point sources. All sources are resolved in the line emission. Only two of them show circumstellar structure (a cavity and a bipolar structure), one shows a very strange brightness distribution (in this context), while the rest have centrally peaked, circular symmetric emission (at 0″.15 resolution). Thirteen objects show Mira-like variability with well-determined periods, seven show non-periodic or very-low-amplitude variability, one show multi-period non-Mira-like variability, while the fluxes are saturated for the remaining object.

Spectral energy distributions have been constructed from extinction-corrected photometry and luminosities have been estimated. This leads to a division (based on luminosity criteria) of our sample into 17 objects that are most likely located in the inner GB, and five objects that are most likely foreground sources. Further, the sub-sample of inner-GB objects is divided into two classes depending on the SED characteristics: eleven objects have standard dust CSEs (SE), while six have detached dust CSEs and indications of warmer central stars (DE). The SE sources all have long-period Mira-like variability, while the DE sources are predominantly non-periodic. A reasonable explanation for this is that the DE sources have evolved further than the SE sources. Most likely they have reached a stage where the mass-loss rate has decreased significantly, and some of them may have already left the AGB, evolving to the left in the Hertzsprung-Russell diagram towards the white dwarf stage. The two sources with resolved circumstellar structure in CO line emission, in both cases in the form of a cavity and a bipolar structure, belong to the DE class and are probably the most evolved. The two classes appear to be rather distinct, and this suggests that the transition from one stage to the other is fast, of the order $\lesssim$100 yr, if our evolutionary interpretation is correct. It is also apparent that, when data at longer wavelengths ($\gtrsim$70 µm) are available, the SED fits are often not very good, the flux densities are underestimated. This applies to ten objects, and it indicates more complex geometries of the dust CSEs, a varying mass-loss-rate history, a possible effects of grain size, and/or the use of inadequate dust optical properties.

For the inner-GB sub-sample, we derived luminosities that imply that the sources (except for two higher-luminosity sources) are lower-mass stars of median mass $\approx$1.2–1.6 $M_\odot$, and a population age of $\approx$4–7 Gyr (the uncertainty depends on the stellar evolution model being used). The two higher-luminosity objects, with estimated masses of $\approx$4.3 $M_\odot$, belong to a much younger population (<1 Gyr), unless they are foreground sources. For the sources with determined variability period, the luminosities are, at least, a factor of two lower than those estimated from commonly used PL relations. This may be interpreted as an effect of

substantial mass loss, lowering the present stellar mass, possibly augmented by a higher metallicity.

Despite the relatively low mass for the inner-GB sub-sample stars, the mass-loss rates are high, a median of $2 \times 10^{-5} \, M_\odot \, \mathrm{yr}^{-1}$, and the CSEs expand at high terminal velocities, a median of $18 \, \mathrm{km \, s^{-1}}$. Consequently, these objects fall on the high-end tail of AGB stellar mass-loss-rate and gas expansion velocity distributions estimated for solar-neighbourhood O-type AGB stars (Ramstedt et al. 2009). The high expansion velocities suggest that our inner-GB sources are not low-metallicity objects. Further, the inner-GB sources have very low estimated circumstellar $^{12}\mathrm{CO}/^{13}\mathrm{CO}$ abundance ratios, a median of five, and by inference very low stellar $^{12}\mathrm{C}/^{13}\mathrm{C}$ isotope ratios. This is theoretically very difficult to understand, since our sources are not expected to go through HBB. Such low ratios can possibly be set during the evolution on the Red Giant Branch if effective extra mixing is present. Unfortunately, our sample size is not large enough to allow a comparison between the luminosities, mass-loss rates, gas expansion velocities, and circumstellar $^{12}\mathrm{CO}/^{13}\mathrm{CO}$ abundance ratios of the SE and DE sources.

The estimated gas-to-dust ratios for the inner-GB SE sources have a median of 200 and quite some spread, in line with what has been reported in other studies of different samples of AGB stars. On the contrary, the estimated low gas-to-dust ratios for the DE sources indicate that the dust-mass-loss rate estimates are wrong, most likely due to the adopted geometry of their dust CSEs being wrong. A further indication of the latter is the uniformity of the dust temperature at the inner radius of the dust CSE, which is difficult to explain within the adopted isotropic dust CSE.

Our data do not allow an observational determination of the CO photodissociation radii of our inner-GB sources. In fact, these radii can be substantially smaller than calculated using Eq. (5), for instance, as a result of a stronger interstellar UV radiation field close to the GC (however, the CO photodissociation radius of a higher-mass-loss-rate object is only moderately sensitive to the strength of the UV field), without affecting the estimated source sizes and mass-loss rates. On the other hand the size of the OH shell is more susceptible to a change in the UV radiation field than is the CO envelope. An OH shell three times smaller than that estimated for a solar neighbourhood interstellar UV radiation field would nicely explain why we have no objects with inner dust-CSE radii larger than $\approx 600 \, \mathrm{au}$. They would not show any OH 1612 MHz emission, and hence would not end up in our sample.

Our CO line radiative transfer modelling fails in two respects. First, the observed $^{12}\mathrm{CO}$ $J = 3\text{--}2/2\text{--}1$ line intensity ratios (primarily determined by the mass-loss rate in the model) are not reproduced in several cases. This could be caused by the limited S/N of the observational data, but it may also indicate that the use of the same circumstellar model for all sources is a too crude approach. Second, the observed presence of extended, low-level, brightness emission in many cases is also not reproduced in the models. There are several possible reasons for this, such as a mass-loss rate varying with time or a non-isotropic CSE.

Three of the foreground sources are likely AGB stars, while the nature of the remaining two is uncertain. We present results for the AGB stars assuming they have a luminosity of $5600 \, L_\odot$, but note that for the two sources with determined periods, this value is significantly below those predicted by PL relations.

In summary we have reached the following conclusions:
– For a sample of 22 OH/IR stars in the direction of the inner GB (within $2°$ of the GC), we detect all in at least one CO

rotational line using ALMA. Eight of them are detected in 324 GHz continuum.
– Periods of Mira-like pulsational variability have been determined for 12 objects, and one period is taken from the literature. They fall in the range about 500–1200 days. Six objects show no periodic variability.
– Based on luminosity criteria, 17 of these objects are believed to be located in the inner GB. The conclusion points below, except the last one, refer to this sub-sample.
– The median luminosity, $5600 \, L_\odot$, corresponds to an initial mass in the range 1.2–1.6 $M_\odot$. Two stars have significantly higher luminosities, $25\,000 \, L_\odot$, suggesting that they are higher-mass stars, or lie in the foreground.
– For the lower-mass stars the luminosities fall well below those predicted by established period-luminosity relations, most likely due to these stars having reached the end of the AGB evolution.
– The objects are further divided into stars that are approaching the tip of the AGB (about two thirds of the objects) and stars that have recently left the AGB. The former stars all show Mira-like variability, while the latter stars show no, or very-low-amplitude, periodic variability. In addition, the latter stars appear to be warmer.
– The median gas-mass-loss rate, gas terminal expansion velocity, gas-to-dust mass ratio, and circumstellar $^{12}\mathrm{CO}/^{13}\mathrm{CO}$ abundance ratio are estimated to be $2 \times 10^{-5} \, M_\odot \, \mathrm{yr}^{-1}$, $18 \, \mathrm{km \, s^{-1}}$, 200 (excluding the sources that have recently left the AGB), and 5, respectively.
– Both the median mass-loss rate and gas expansion velocity lie at the high end of values found for AGB stars. The latter can be taken as an indication that these stars are not low-metallicity objects.
– The low circumstellar $^{12}\mathrm{CO}/^{13}\mathrm{CO}$ abundance ratios, and hence inferred stellar $^{12}\mathrm{C}/^{13}\mathrm{C}$ isotope ratios, are most likely produced through efficient dredge-up on the RGB.
– Resolved structure in the CO line brightness distributions are seen for only two sources. These belong to the group of stars that are believed to have left the AGB.
– It is unlikely that the UV radiation field in the inner GB is so high that it has any effect on our estimated mass-loss rates and $^{12}\mathrm{CO}/^{13}\mathrm{CO}$ abundance ratios. On the contrary, the OH shell size is more sensitive to the strength of the UV radiation field, and this may explain why there are no sources in our sample with an inner radius of the dust CSE larger than 600 au.
– Our circumstellar CO line radiative transfer modelling fails in two respects. The observed $^{12}\mathrm{CO}$ $J = 3\text{--}2/2\text{--}1$ line intensity ratios are not reproduced in several cases. The observed presence of extended, low-level, brightness emission in many cases is also not reproduced in the models.
– Finally, the remaining five sources are likely foreground objects. Three are likely AGB stars, while the nature of two is uncertain.

More firmly establishing the findings presented in this paper requires the observations of a larger sample of inner-GB OH/IR stars (in particular of the DE type) in more $^{12}\mathrm{CO}$ lines (to significantly improve the circumstellar model and the gas-mass-loss-rate estimates), in more $^{13}\mathrm{CO}$ lines (to significantly improve the estimates of the circumstellar $^{12}\mathrm{CO}/^{13}\mathrm{CO}$ abundance ratio), and in continuum (to put better constraints on the long-wavelength behaviour of the SEDs). Given that our data on a sample of 22 stars were obtained with a short observing time, it is certainly feasible to achieve such an improvement within a reasonable

amount of observing time. Such a sample of equidistant sources would be excellent for studying the evolution of the mass-loss characteristics of solar-type stars at the tip, and slightly beyond, the AGB.

References

Abrahamyan, H. V., Mickaelian, A. M., & Knyazyan, A. V. 2015, Astron. Comput., 10, 99

Agúndez, M., Martínez, J. I., de Andres, P. L., Cernicharo, J., & Martín-Gago, J. A. 2020, A&A, 637, A59

Barbuy, B., Chiappini, C., & Gerhard, O. 2018, ARA&A, 56, 223

Baud, B., & Habing, H. J. 1983, A&A, 127, 73

Baud, B., Habing, H. J., Matthews, H. E., & Winnberg, A. 1981, A&A, 95, 156

Bernes, C. 1979, A&A, 73, 67

Blommaert, J. A. D. L., van der Veen, W. E. C. J., van Langevelde, H. J., Habing, H. J., & Sjouwerman, L. O. 1998, A&A, 329, 991

Blommaert, J. A. D. L., Groenewegen, M. A. T., Justtanont, K., & Decin, L. 2018, MNRAS, 479, 3545

Bowers, P. F. 1978, A&A, 64, 307

Braga, V. F., Contreras Ramos, R., Minniti, D., et al. 2019, A&A, 625, A151

Caswell, J. L., & Haynes, R. F. 1975, MNRAS, 173, 649

Chambers, K. C., & Pan-STARRS Team. 2016, in American Astronomical Society Meeting Abstracts, 227, 324.07

Chen, P. S., Szczerba, R., Kwok, S., & Volk, K. 2001, A&A, 368, 1006

Clayton, D. D., & Nittler, L. R. 2004, ARA&A, 42, 39

Cohen, R. J., Downs, G., Emerson, R., et al. 1987, MNRAS, 225, 491

Cutri, R. M., Wright, E. L., Conrow, T., et al. 2013, VizieR Online Data Catalog: II/328

Danilovich, T., Van de Sande, M., De Beck, E., et al. 2017, A&A, 606, A124

De Beck, E., Decin, L., de Koter, A., et al. 2010, A&A, 523, A18

Decin, L., Homan, W., Danilovich, T., et al. 2019, Nat. Astron., 3, 408

Deguchi, S. 1982, ApJ, 259, 634

Delfosse, X., Kahane, C., & Forveille, T. 1997, A&A, 320, 249

De Nutte, R., Decin, L., Olofsson, H., et al. 2017, A&A, 600, A71

Eder, J., Lewis, B. M., & Terzian, Y. 1988, ApJS, 66, 183

Egan, M. P., Price, S. D., Kraemer, K. E., et al. 2003, VizieR Online Data Catalog: V/114

Elia, D., Molinari, S., Schisano, E., et al. 2017, MNRAS, 471, 100

Elitzur, M., Goldreich, P., & Scoville, N. 1976, ApJ, 205, 384

Engels, D., & Lewis, B. M. 1996, A&As, 116, 117

Gaia Collaboration (Brown, A. G. A., et al.). 2021, A&A, 649, A1

García Pérez, A. E., Ness, M., Robin, A. C., et al. 2018, ApJ, 852, 91

Gilroy, K. K. 1989, ApJ, 347, 835

Gilroy, K. K., & Brown, J. A. 1991, ApJ, 371, 578

Glass, I. S., Matsumoto, S., Carter, B. S., & Sekiguchi, K. 2001, MNRAS, 321, 77

Goldman, S. R., van Loon, J. T., Zijlstra, A. A., et al. 2017, MNRAS, 465, 403

Goldreich, P., & Scoville, N. 1976, ApJ, 205, 144

González Delgado, D., Olofsson, H., Kerschbaum, F., et al. 2003, A&A, 411, 123

Gonzalez, O. A., Minniti, D., Valenti, E., et al. 2018, MNRAS, 481, L130

Gravity Collaboration (Abuter, R., et al.). 2019, A&A, 625, L10

Groenewegen, M. A. T. 2022, A&A, 659, A145

Groenewegen, M. A. T., & Blommaert, J. A. D. L. 2005, A&A, 443, 143

Groenewegen, M. A. T., Vlemmings, W. H. T., Marigo, P., et al. 2016, A&A, 596, A50

Groenewegen, M. A. T., Nanni, A., Cioni, M. R. L., et al. 2020, A&A, 636, A48

Gutermuth, R. A., & Heyer, M. 2015, AJ, 149, 64

Habing, H. J. 1996, A&Ar, 7, 97

Hackstein, M., Fein, C., Haas, M., et al. 2015, Astronomische Nachrichten, 336, 590

Herschel Point Source Catalogue Working Group, Marton, G., Calzoletti, L., et al. 2020, VizieR Online Data Catalog: VIII/106

Heske, A., Habing, H. J., Forveille, T., Omont, A., & van der Veen, W. E. C. J. 1990, A&A, 239, 173

Hinkle, K. H., Lebzelter, T., & Straniero, O. 2016, ApJ, 825, 38

Hinz, J. L., Rieke, G. H., Yusef-Zadeh, F., et al. 2009, VizieR Online Data Catalog: J/ApJS/181/227

Höfner, S., & Olofsson, H. 2018, A&Ar, 26, 1

Huggins, P. J., & Glassgold, A. E. 1982, AJ, 87, 1828

Ishihara, D., Onaka, T., Kataza, H., et al. 2010, A&A, 514, A1

Jiménez-Esteban, F. M., & Engels, D. 2015, A&A, 579, A76

Johansson, L. E. B., Andersson, C., Goss, W. M., & Winnberg, A. 1977, A&A, 54, 323

Justtanont, K., & Tielens, A. G. G. M. 1992, ApJ, 389, 400

Justtanont, K., Skinner, C. J., & Tielens, A. G. G. M. 1994, ApJ, 435, 852

Justtanont, K., Skinner, C. J., Tielens, A. G. G. M., Meixner, M., & Baas, F. 1996, ApJ, 456, 337

Justtanont, K., Barlow, M. J., Blommaert, J., et al. 2015, A&A, 578, A115

Karakas, A. I. 2014, MNRAS, 445, 347

Karakas, A. I., & Lattanzio, J. C. 2014, PASA, 31, e030

Karakas, A. I., & Lugaro, M. 2016, ApJ, 825, 26

Kormendy, J., & Bender, R. 2019, ApJ, 872, 106

Kwok, S. 1975, ApJ, 198, 583

Le Bertre, T. 1993, A&As, 97, 729

Le Squeren, A. M., Sivagnanam, P., Dennefeld, M., & David, P. 1992, A&A, 254, 133

Lindqvist, M., Habing, H. J., & Winnberg, A. 1992a, A&A, 259, 118

Lindqvist, M., Winnberg, A., Habing, H. J., & Matthews, H. E. 1992b, A&As, 92, 43

Lucas, P. W., Hoare, M. G., Longmore, A., et al. 2008, MNRAS, 391, 136

Mainzer, A., Bauer, J., Grav, T., et al. 2011, ApJ, 731, 53

Mainzer, A., Bauer, J., Cutri, R. M., et al. 2014, ApJ, 792, 30

Matsunaga, N., Kawadu, T., Nishiyama, S., et al. 2009, MNRAS, 399, 1709

McClure, M. 2009, ApJ, 693, L81

McMullin, J. P., Waters, B., Schiebel, D., Young, W., & Golap, K. 2007, in Astronomical Society of the Pacific Conference Series, Astronomical Data Analysis Software and Systems XVI, eds. R. A. Shaw, F. Hill, & D. J. Bell, 376, 127

Mezger, P. G., Duschl, W. J., & Zylka, R. 1996, A&Ar, 7, 289

Milam, S. N., Savage, C., Brewster, M. A., Ziurys, L. M., & Wyckoff, S. 2005, ApJ, 634, 1126

Min, M., Dullemond, C. P., Dominik, C., de Koter, A., & Hovenier, J. W. 2009, A&A, 497, 155

Minniti, D., Lucas, P. W., Emerson, J. P., et al. 2010, New A, 15, 433

Molinari, S., Schisano, E., Elia, D., et al. 2016, A&A, 591, A149

Netzer, N., & Knapp, G. R. 1987, ApJ, 323, 734

Nishiyama, S., Tamura, M., Hatano, H., et al. 2009, ApJ, 696, 1407

Ochsenbein, F., Bauer, P., & Marcout, J. 2000, A&As, 143, 23

Olivier, E. A., Whitelock, P., & Marang, F. 2001, MNRAS, 326, 490

Olofsson, H., González Delgado, D., Kerschbaum, F., & Schöier, F. 2002, A&A, 391, 1053

Omont, A., Gilmore, G. F., Alard, C., et al. 2003, A&A, 403, 975

Ossenkopf, V., Henning, T., & Mathis, J. S. 1992, A&A, 261, 567

Ramstedt, S., & Olofsson, H. 2014, A&A, 566, A145
Ramstedt, S., Schöier, F. L., Olofsson, H., & Lundgren, A. A. 2008, A&A, 487, 645
Ramstedt, S., Schöier, F. L., & Olofsson, H. 2009, A&A, 499, 515
Ramstedt, S., Vlemmings, W. H. T., Doan, L., et al. 2020, A&A, 640, A133
Saberi, M., Vlemmings, W. H. T., & De Beck, E. 2019, A&A, 625, A81
Saberi, M., Olofsson, H., Vlemmings, W. H. T., et al. 2020, A&A, 638, A99
Sargent, B. A., Srinivasan, S., & Meixner, M. 2011, ApJ, 728, 93
Sargent, B. A., Patel, N. A., Meixner, M., et al. 2013, ApJ, 765, 20
Sawada, T., Hasegawa, T., Handa, T., et al. 2001, ApJS, 136, 189
Schöier, F. L., & Olofsson, H. 2001, A&A, 368, 969
Schöier, F. L., Ramstedt, S., Olofsson, H., et al. 2013, A&A, 550, A78
Schultheis, M., Rojas-Arriagada, A., Cunha, K., et al. 2020, A&A, 642, A81
Sevenster, M. N. 2002, AJ, 123, 2772
Sevenster, M. N., Chapman, J. M., Habing, H. J., Killeen, N. E. B., & Lindqvist, M. 1997, A&As, 122, 79
Sjouwerman, L. O., van Langevelde, H. J., Winnberg, A., & Habing, H. J. 1998, A&As, 128, 35
Soszyński, I., Udalski, A., Szymański, M. K., et al. 2013, Acta Astron., 63, 21
Spitzer Science, C. 2009, VizieR Online Data Catalog: II/293
te Lintel Hekkert, P., Caswell, J. L., Habing, H. J., et al. 1991, A&As, 90, 327
Tsuji, T. 2007, in IAU Symposium, Convection in Astrophysics, eds. F. Kupka, I. Roxburgh, & K. L. Chan, 239, 307
Uscanga, L., Gómez, J. F., Suárez, O., & Miranda, L. F. 2012, A&A, 547, A40

van der Veen, W. E. C. J., & Habing, H. J. 1990, A&A, 231, 404
van Dishoeck, E. F. 1988, in Astrophysics and Space Science Library, Rate Coefficients in Astrochemistry, eds. T. J. Millar, & D. A. Williams, 146, 49
van Loon, J. T., Gilmore, G. F., Omont, A., et al. 2003, MNRAS, 338, 857
Vassiliadis, E., & Wood, P. R. 1993, ApJ, 413, 641
Ventura, P., Karakas, A., Dell'Agli, F., García-Hernández, D. A., & Guzman-Ramirez, L. 2018, MNRAS, 475, 2282
Wang, S., Li, A., & Jiang, B. W. 2015, ApJ, 811, 38
Watson, W. D., Anicich, V. G., & Huntress, W. T., J. 1976, ApJ, 205, L165
Whitelock, P., Feast, M., & Catchpole, R. 1991, MNRAS, 248, 276
Wiegert, J., Groenewegen, M. A. T., Jorissen, A., Decin, L., & Danilovich, T. 2020, A&A, 642, A142
Wilson, W. J., & Barrett, A. H. 1972, A&A, 17, 385
Winnberg, A., Goss, W. M., Höglund, B., & Johansson, L. E. B. 1973, Astrophys. Lett., 13, 125
Winnberg, A., Lindqvist, M., Olofsson, H., & Henkel, C. 1991, A&A, 245, 195
Winnberg, A., Deguchi, S., Reid, M. J., et al. 2009, A&A, 497, 177
Wood, P. R., Habing, H. J., & McGregor, P. J. 1998, A&A, 336, 925
Wright, E. L., Eisenhardt, P. R. M., Mainzer, A. K., et al. 2010, AJ, 140, 1868
Xue, M., Jiang, B. W., Gao, J., et al. 2016, ApJS, 224, 23
Yang, B., Stancil, P. C., Balakrishnan, N., & Forrey, R. C. 2010, ApJ, 718, 1062
Zacharias, N., Monet, D. G., Levine, S. E., et al. 2005, VizieR Online Data Catalog: I/297
Zijlstra, A. A., te Lintel Hekkert, P., Pottasch, S. R., et al. 1989, A&A, 217, 157

Appendix A: Observational results

Appendix A.1. Tables

Tables with the observational results for the ^{12}CO($J = 2$–1 and 3–2), ^{13}CO($J = 3$–2), and H^{13}CN($J = 4$–3) lines, and the 222, 324, and 339 GHz continuum data are presented here.

Table A.1. Results for the ^{12}CO $J = 2$–1 line.

Source	S [a] [Jy]	$\int S\,dv$ [Jy km s^{-1}]	v_c [b] [km s^{-1}]	v_∞ [b] [km s^{-1}]	β	θ_s [c] ['']	Remarks
1 - OH358.083+0.137	0.35	8.7	−24	19	0.5	0.38	Low S/N
2 - OH358.162+0.490	6.0	250	3	20	0.0	1.46	
3 - OH358.235+0.115	0.45	14	−25	19	0.0	0.63	
4 - OH358.505+0.330	1.5	31	−30	25	−0.5	0.70	$B > 25$ m data used
5 - OH359.140+1.137	0.78	12	−137	11	0.5	0.44	
6 - OH359.149−0.043	0.31	11	53	27	1.0	. . .	$B > 50$ m data used; Brightness distr.?
7 - OH359.220+0.163	2.3	50	−138	15	0.5	1.25	Resolved structure
8 - OH359.233−1.876	0.98	23	−16	17	0.5	0.60	
9 - OH359.467+1.029	0.30	11	110	16	0.5	0.58	
10 - OH359.543−1.775	0.15	7.3	95	32	0.5	0.31	Low S/N
11 - OH359.664+0.636	0.91	16	−158	13	0.5	0.84	
12 - OH359.745−0.404	0.44	9.9	184	22	0.5	0.69	
13 - OH359.805+0.200	0.22	2.9	−48	15	0.3	. . .	$B > 25$ m data used; Low S/N
14 - OH359.826+0.153	0.12	2.5	−26	16	0.3	0.51	$B > 50$ m data used; Low S/N
15 - OH359.902+0.061	0.51	8.4	−123	13	0.5	0.43	$B > 25$ m data used; Low S/N
16 - OH0.173+0.211	0.31	7.5	52	18	1.0	0.52	$B > 25$ m data used
17 - OH0.221+0.168	0.13	4.9	60	26	1.0	0.44	$B > 50$ m data used
18 - OH0.548−0.059	0.10	2.0	−53	22	−0.5	0.59	$B > 50$ m data used; Low S/N
19 - OH0.739+0.411	0.81	13	−21	12	0.3	1.04	$B > 25$ m data used; Line profile?
20 - OH1.095−0.832	2.1	104	10	23	−0.3	0.91	
21 - OH1.221+0.294	2.2	44	−261	14	0.5	0.57	
22 - OH1.628+0.617	0.86	34	−84	30	1.0	0.80	

Notes. [a] See text for details on the uncertainties of the flux densities, but we estimate that for lines stronger than 1.0 Jy the uncertainty is about 10%, while for lines weaker than 0.4 Jy the uncertainty increases to about 50% for the weakest lines. [b] The uncertainties in the expansion and centre velocities are estimated to be about ± 2 and ± 1.5 km s^{-1}, respectively. [c] Average of the deconvolved major and minor axes of a two-dimensional Gaussian fit to the brightness distribution.

Table A.2. Results for the ^{12}CO $J = 3$–2 line.

Source	S [a] [Jy]	$\int S\,dv$ [Jy km s^{-1}]	v_c [b] [km s^{-1}]	v_∞ [b] [km s^{-1}]	β	θ_s [c] ['']	Remarks
1 - OH358.083+0.137	0.68	20	−23	21	0.5	0.52	Low S/N
2 - OH358.162+0.490	9.4	320	4	26	0.5	0.70	
3 - OH358.235+0.115	0.91	32	−21	19	0.0	0.46	Low S/N
4 - OH358.505+0.330	2.2	57	−34	27	−0.2	. . .	Low S/N
5 - OH359.140+1.137	0.26	5.2	−134	13	0.0	. . .	$B > 25$ m data used
6 - OH359.149−0.043	2.0	57	47	27	1.0	. . .	$B > 25$ m data used; Brightness distr.?
7 - OH359.220+0.163	2.1	40	−139	13	0.5	1.26	Brightness distr.?
8 - OH359.233−1.876	0.65	15	−11	21	0.5	0.31	Low S/N
9 - OH359.467+1.029	0.74	18	110	15	0.5	0.58	Low S/N
10 - OH359.543−1.775	0.18	8.4	90	37	0.5	0.27	Low S/N
11 - OH359.664+0.636	0.28	4.8	−158	14	0.5	. . .	Low S/N
12 - OH359.745−0.404	0.25	6.4	189	20	0.5	. . .	$B > 25$ m data used; Low S/N
13 - OH359.805+0.200	<0.3	. . .	. . .	. . .	. . .	. . .	
14 - OH359.826+0.153	0.25	6.7	−26	19	0.0	. . .	
15 - OH359.902+0.061	0.29	6.5	−129	11	0.5	0.24	Low S/N
16 - OH0.173+0.211	<0.6	. . .	. . .	. . .	. . .	. . .	
17 - OH0.221+0.168	0.85	13	66	15	0.5	0.31	$B > 25$ m data used; Low S/N
18 - OH0.548−0.059	0.45	8.6	−47	23	0.0	0.35	$B > 50$ m data used; Low S/N
19 - OH0.739+0.411	1.3	27	−21	15	0.5	0.33	$B > 25$ m data used
20 - OH1.095−0.832	1.8	86	11	22	0.0	0.83	
21 - OH1.221+0.294	3.0	43	−261	10	0.5	. . .	
22 - OH1.628+0.617	0.45	15	−87	25	0.0	. . .	

Notes. [a] The upper limits are 3σ. See text for details on the uncertainties of the flux densities, but we estimate that for lines stronger than 2.0 Jy the uncertainty is about 10%, while for lines weaker than 1.0 Jy the uncertainty increases to about 50% for the weakest lines. [b] The uncertainties in the expansion and centre velocities are estimated to be about ± 3 and ± 2 km s^{-1}, respectively. [c] Average of the deconvolved major and minor axes of a two-dimensional Gaussian fit to the brightness distribution.

Table A.3. Results for the ^{13}CO $J = 3$–2 line.

Source	S [a] [Jy]	$\int S\,dv$ [Jy km s^{-1}]	v_c [b] [km s^{-1}]	v_∞ [b] [km s^{-1}]	β	θ_s [c] ['']	Remarks
1 - OH358.083+0.137	0.18	6.4	−26	26	0.5	0.37	
2 - OH358.162+0.490	1.7	74	2	23	0.0	0.72	
3 - OH358.235+0.115	0.04	2.2	−17	18	0.0	0.16	Low S/N
4 - OH358.505+0.330	0.91	25	−26	20	0.5	0.93	Resolved structure
5 - OH359.140+1.137	0.19	3.1	−135	12	0.5	0.27	
6 - OH359.149−0.043	0.28	3.1	46	25	1.0	...	$B > 25$ m data used; Brightness distr.?
7 - OH359.220+0.163	0.51	16	−135	19	0.3	0.72	Resolved structure
8 - OH359.233−1.876	0.24	6.3	−15	18	0.5	0.28	
9 - OH359.467+1.029	0.10	2.8	110	23	0.5	0.43	
10 - OH359.543−1.775	0.13	6.7	87	40	0.5	0.24	Line profile?
11 - OH359.664+0.636	0.10	1.9	−157	13	0.5	0.35	
12 - OH359.745−0.404	0.13	3.9	186	20	0.5	0.34	
13 - OH359.805+0.200	0.05	1.4	−51	21	0.3	0.32	Low S/N
14 - OH359.826+0.153	0.05	1.5	−25	16	0.0	0.35	Low S/N
15 - OH359.902+0.061	0.06	2.2	−133	19	0.0	0.37	$B > 25$ m data used; Low S/N
16 - OH0.173+0.211	<0.08	...	...	...	...	...	
17 - OH0.221+0.168	0.05	1.9	67	27	1.0	0.36	$B > 25$ m data used; Low S/N
18 - OH0.548−0.059	0.15	6.0	−45	31	0.5	0.37	$B > 50$ m data used; Line profile?
19 - OH0.739+0.411	0.58	9.2	−21	10	0.5	0.50	Line profile?
20 - OH1.095−0.832	0.60	33	12	33	−0.3	0.64	
21 - OH1.221+0.294	0.11	4.1	−258	17	0.0	0.31	
22 - OH1.628+0.617	0.03	2.1	−87	25	−0.3	0.22	Low S/N

Notes. [a] The upper limit is 3σ. See text for details on the uncertainties of the flux densities, but we estimate that for lines stronger than 0.2 Jy the uncertainty is about 10%, while for lines weaker than 0.1 Jy the uncertainty increases to about 50% for the weakest lines. [b] The uncertainties in the expansion and centre velocities are estimated to be about ± 1.5 and ± 1 km s^{-1}, respectively. [c] Average of the deconvolved major and minor axes of a two-dimensional Gaussian fit to the brightness distribution.

Table A.4. Results for the H^{13}CN $J = 4$–3 line.

Source	S [a] [Jy]	$\int S\,dv$ [Jy km s^{-1}]	v_c [b] [km s^{-1}]	v_∞ [b] [km s^{-1}]	β	θ_s [c] ['']	Remarks
2 - OH358.162+0.490	1.5	50	3	25	1.0	0.31	
3 - OH358.235+0.115	0.29	12	−15	21	1.0	0.28	Low S/N
20 - OH1.095−0.832	0.16	6.2	10	28	1.0	...	Low S/N

Notes. [a] See text for details on the uncertainties of the flux densities, but we estimate that for lines stronger than 1.0 Jy the uncertainty is about 10%, while for lines weaker than 0.5 Jy the uncertainty increases to about 50%. [b] The uncertainties in the expansion and centre velocities are estimated to be about ± 3 and ± 2 km s^{-1}, respectively. [c] Average of the deconvolved major and minor axes of a two-dimensional Gaussian fit to the brightness distribution.
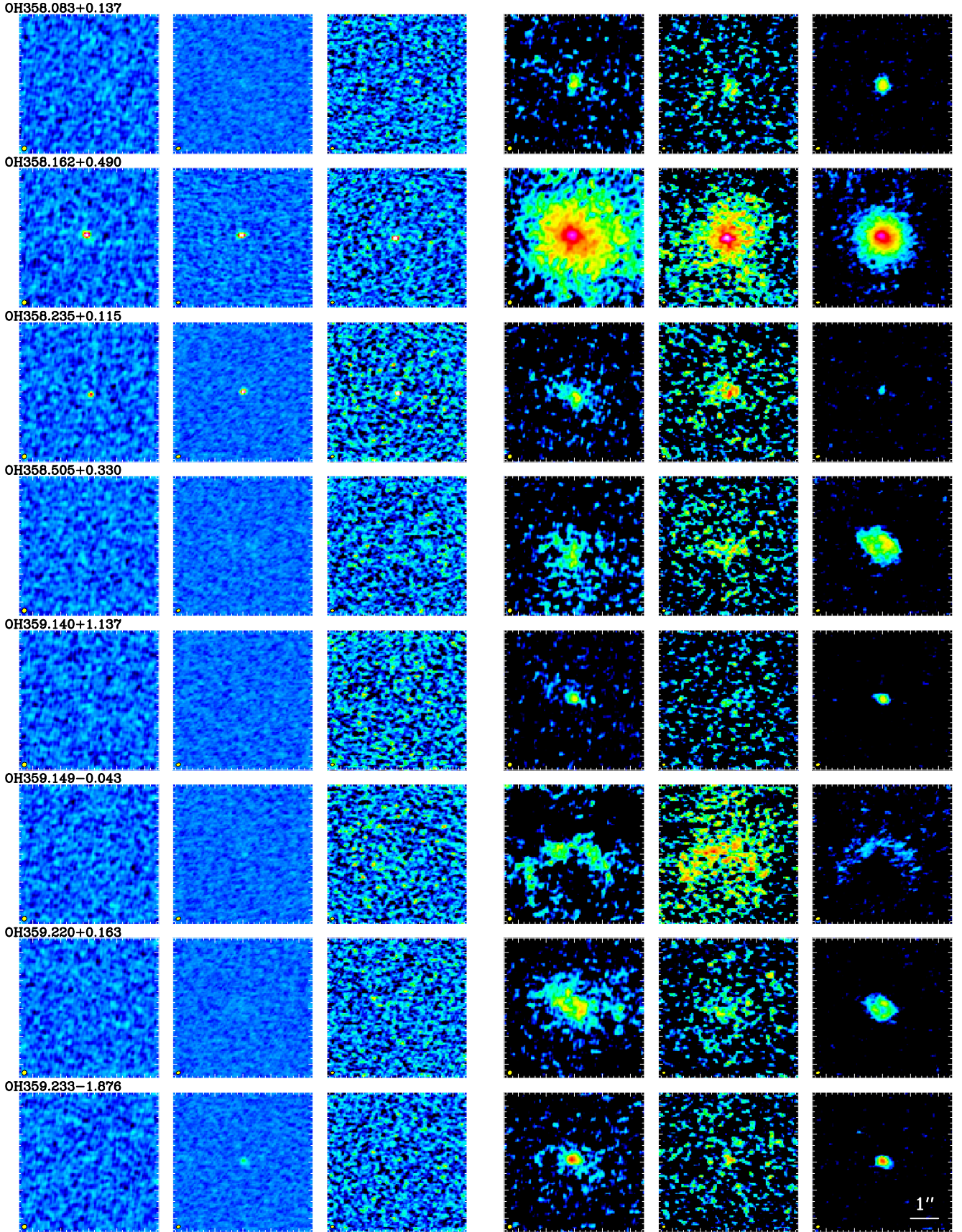
Table A.5. Results of the ALMA continuum observations at 222, 324, and 339 GHz.

Source	$S^{(a)}$			$\theta_s^{(b)}$
	222	324	339	
		[mJy]		[″]
1 - OH358.083+0.137	< 0.8	< 0.4	< 1.8	...
2 - OH358.162+0.490	9.4	11	15	0.10
3 - OH358.235+0.115	4.1	6.8	11	0.06
4 - OH358.505+0.330	< 0.8	< 0.4	< 2.0	...
5 - OH359.140+1.137	< 0.8	< 0.4	< 2.2	...
6 - OH359.149−0.043	< 0.7	0.7	< 2.3	...
7 - OH359.220+0.163	< 0.7	< 0.4	< 1.8	...
8 - OH359.233−1.876	< 0.8	3.6	< 1.8	0.17
9 - OH359.467+1.029	< 0.8	< 0.4	< 2.3	...
10 - OH359.543−1.775	< 0.7	< 0.4	< 1.7	...
11 - OH359.664+0.636	< 0.7	< 0.4	< 2.3	...
12 - OH359.745−0.404	< 0.7	< 0.4	< 2.2	...
13 - OH359.805+0.200	< 0.8	< 0.4	< 1.7	...
14 - OH359.826+0.153	< 0.6	< 0.4	< 1.6	...
15 - OH359.902+0.061	< 0.7	< 0.4	< 2.1	...
16 - OH0.173+0.211	< 1.0	< 0.6	< 3.3	...
17 - OH0.221+0.168	< 0.7	< 0.4	< 1.8	...
18 - OH0.548−0.059	7.8	12	16	0.14
19 - OH0.739+0.411	1.5	4.0	< 1.8	0.12
20 - OH1.095−0.832	8.3	14	15	0.13
21 - OH1.221+0.294	< 0.7	< 0.4	< 1.6	...
22 - OH1.628+0.617	< 0.7	1.0	< 1.7	...

Notes. $^{(a)}$ Flux densities obtained through a fit of a two-dimensional Gaussian to the brightness distribution. The 1σ uncertainties in the flux densities are estimated to be 0.6, 0.5, and 2.0 mJy at 222, 324, and 339 GHz, respectively. The upper limits are 3σ values. $^{(b)}$ Average of the deconvolved major and minor axes of a two-dimensional Gaussian fit to the 324 GHz brightness distribution.

Appendix A.2. Images

Images with the observational results for the ^{12}CO($J = 2$–1 and 3–2) and ^{13}CO($J = 3$–2) lines, and the 222, 324, and 339 GHz continuum data are presented here, as well as the positions of the CO brightness distributions plotted on Spitzer IRAC images.

OH358.083+0.137

OH358.162+0.490

OH358.235+0.115

OH358.505+0.330

OH359.140+1.137

OH359.149−0.043

OH359.220+0.163

OH359.233−1.876

1″

Fig. A.1. Continuum images at 222, 324, and 339 GHz in the 1st, 2nd, and 3rd column, respectively. The ^{12}CO($J=2$–1), ^{12}CO($J=3$–2), and ^{13}CO($J=3$–2) brightness distributions integrated over the velocity range of the line in the 4th, 5th, and 6th column, respectively. Logarithmic scales are used in order to have the same scale for all objects. The image sizes are $5'' \times 5''$. The synthesised beams are shown in the lower left corner of each panel.

OH359.467+1.029

OH359.543−1.775

OH359.664+0.636

OH359.745−0.404

OH359.805+0.200

OH359.826+0.153

OH359.902+0.061

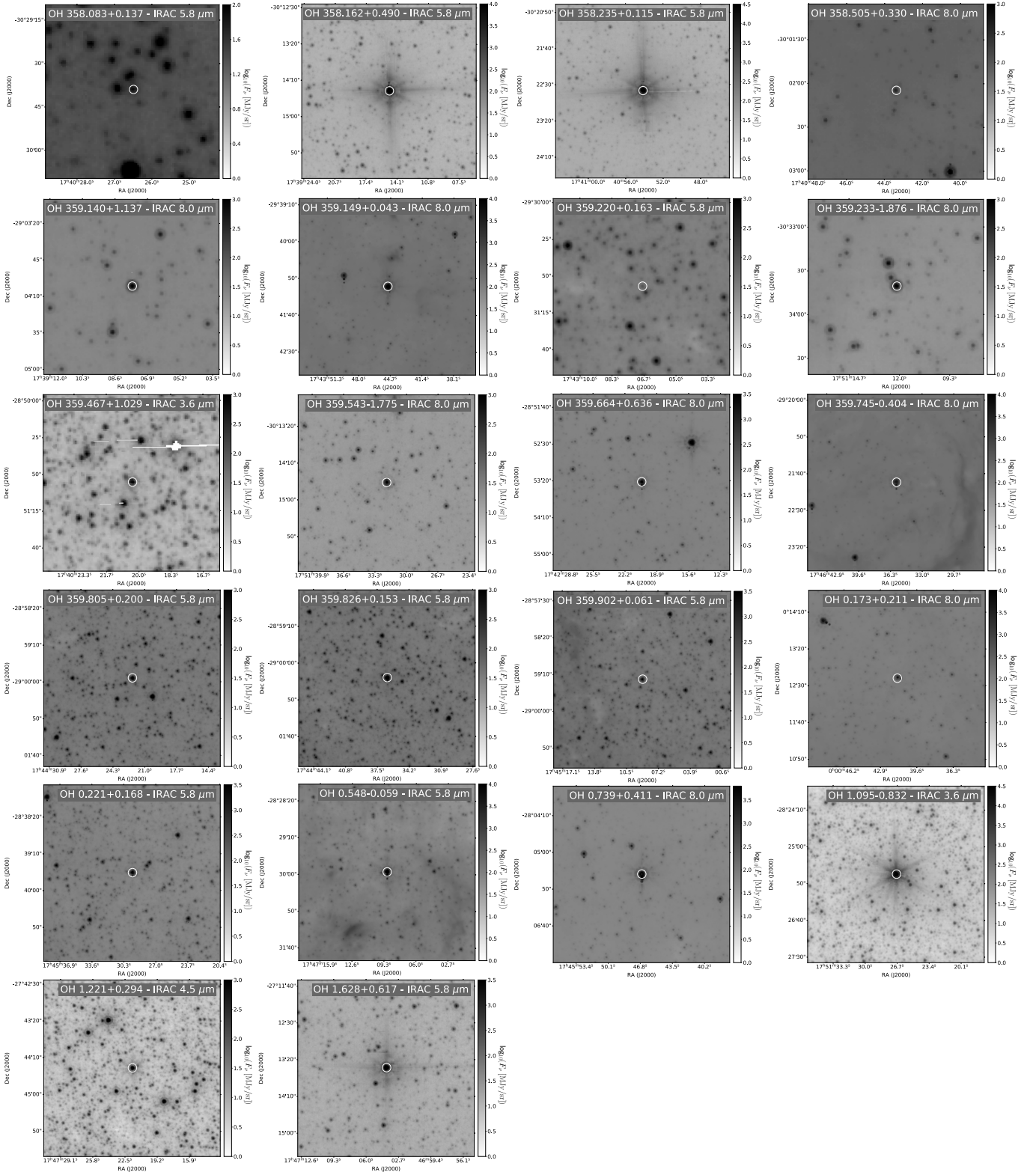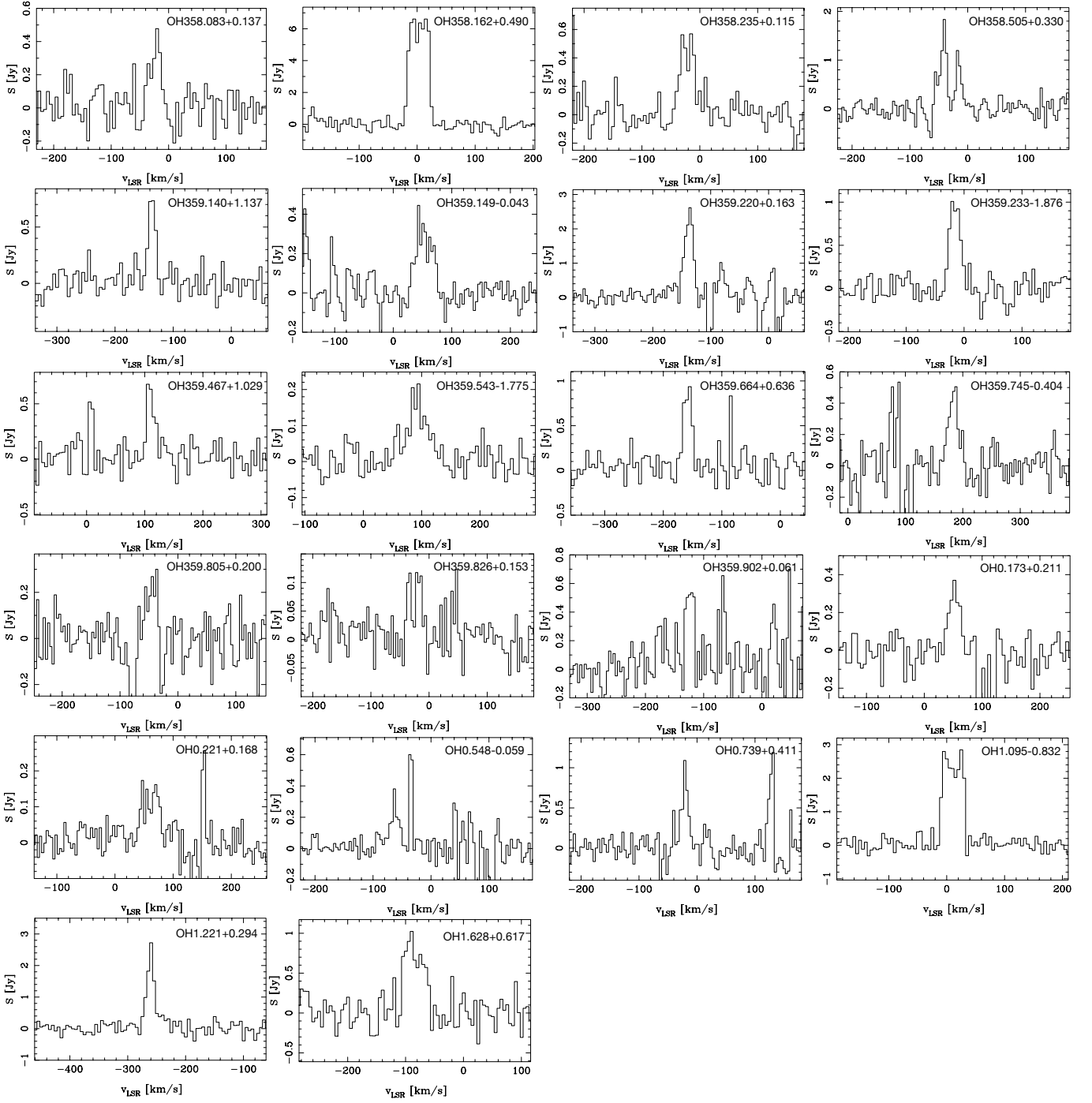OH0.173+0.211

1″
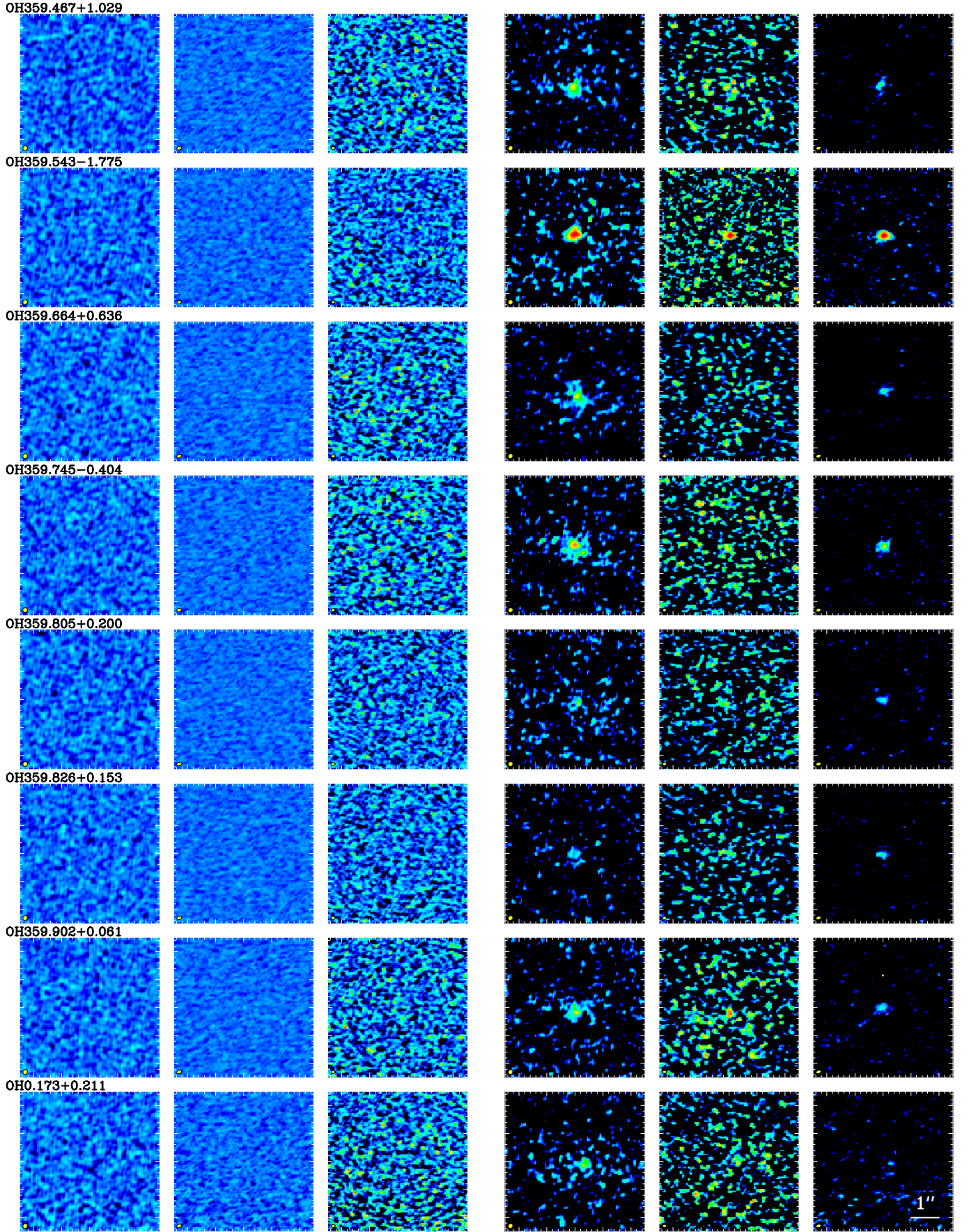
Fig. A.2. Figure A.1 continued.
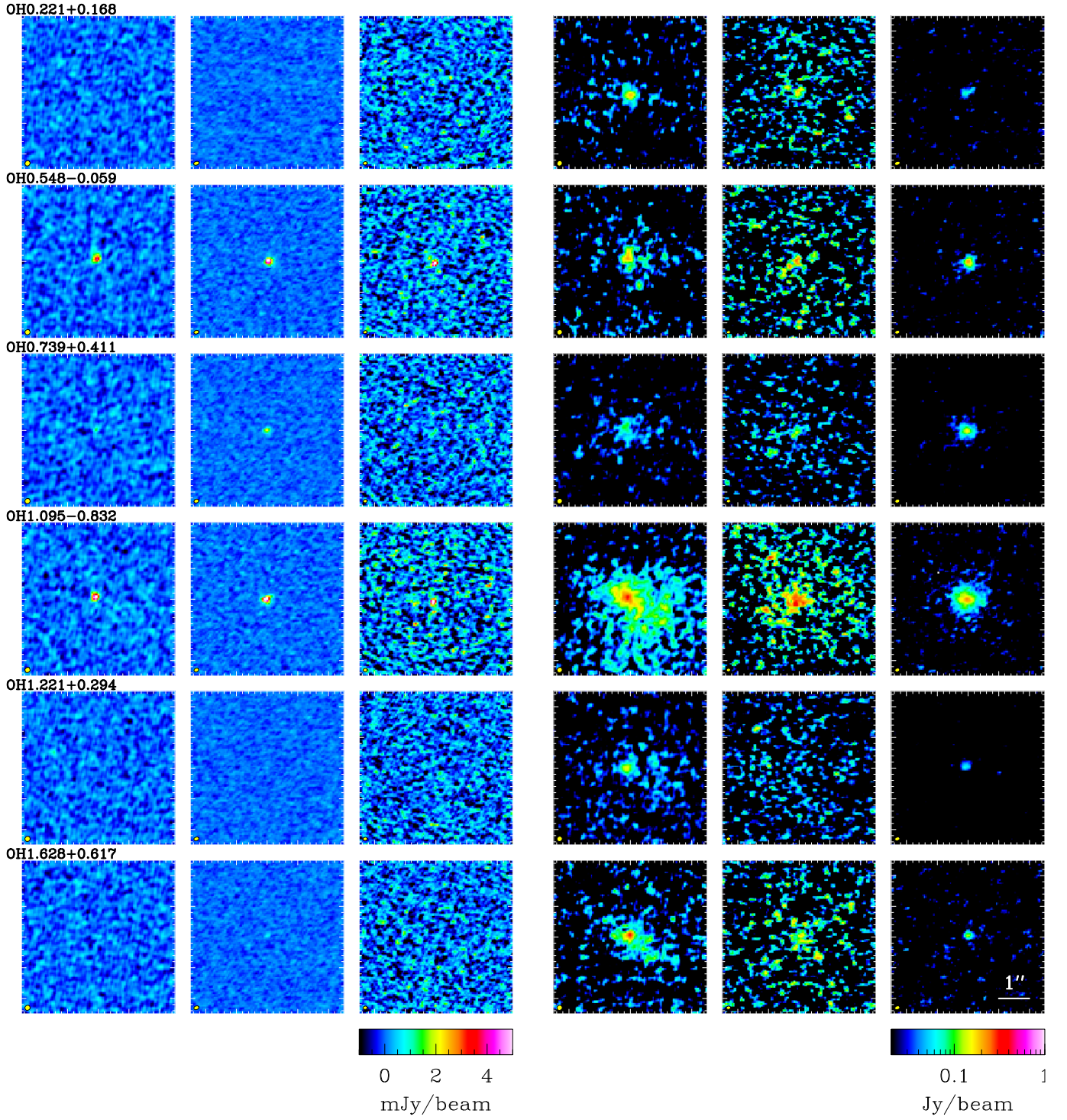
Fig. A.3. Figure A.1 continued.

Fig. A.4. Central position of the ^{13}CO($J = 3$–2) brightness distribution (marked with a white circle) on a Spitzer IRAC 3.6, 4.5, 5.8, or 8.0 μm image [for OH0.173+0.211 the position of the ^{12}CO($J = 2$–1) brightness distribution is used, and for OH359.149+0.043 the position of the 324 GHz continuum peak is used]. The size of the CO line brightness distribution is significantly smaller than the white circle in all cases.
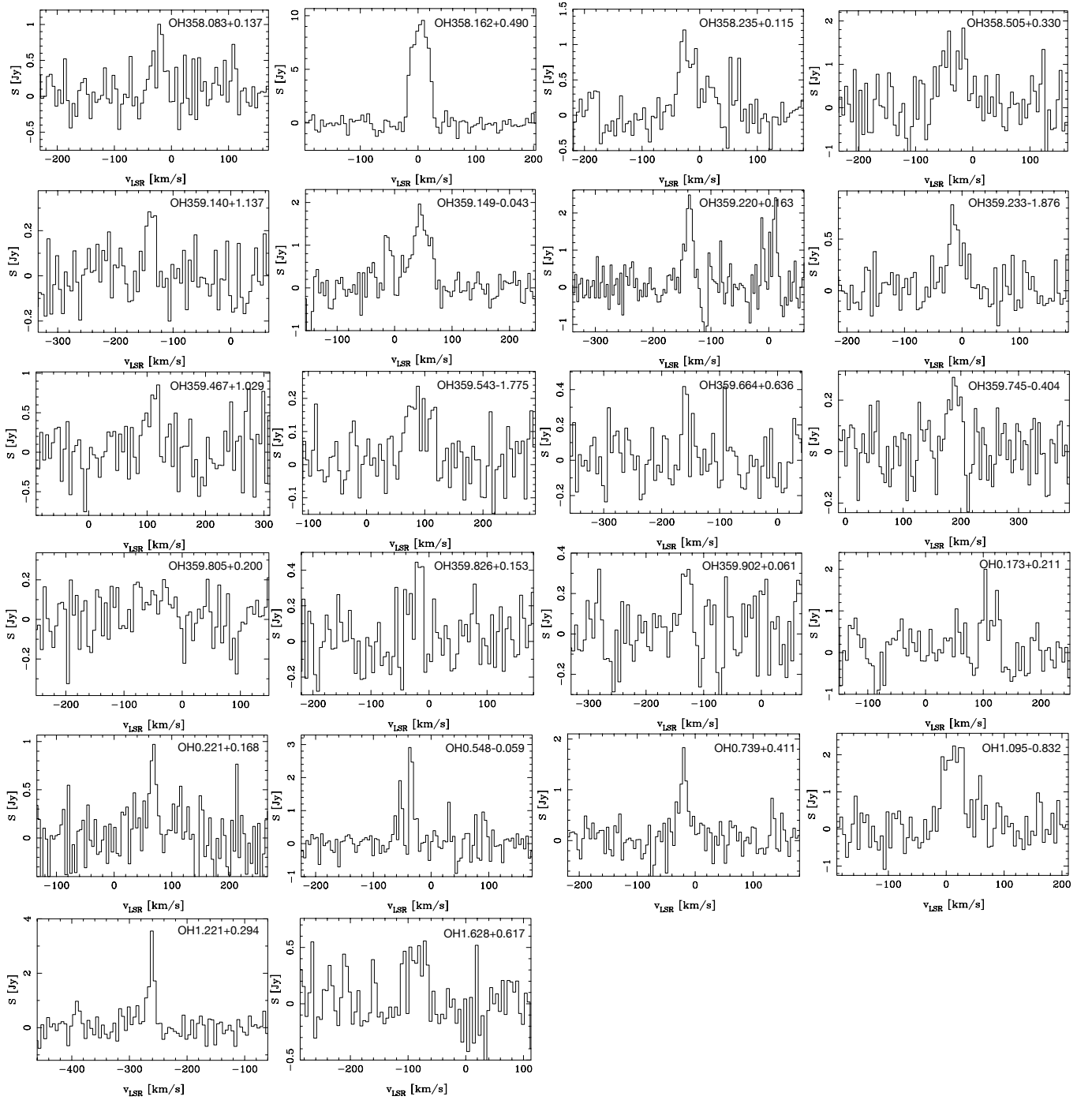
Appendix A.3. Spectra

Spectra of the ^{12}CO($J = 2$–1 and 3–2) and H^{13}CN($J = 4$–3) lines
are presented here.
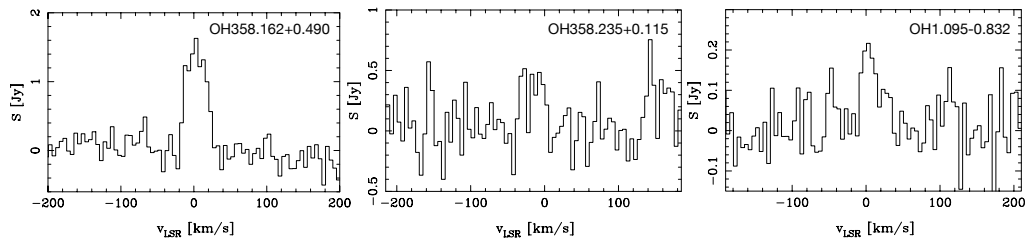
Fig. A.5. $^{12}CO(J=2-1)$ spectra at a velocity resolution of $5\,km\,s^{-1}$.

Fig. A.6. ^{12}CO($J = 3$–2) spectra at a velocity resolution of 5 km s^{-1}. OH359.805+0.200 and OH0.173+0.211 were not detected in this line.

Fig. A.7. H^{13}CN($J = 4$–3) spectra at a velocity resolution of 5 km s^{-1}.